Explaining neural networks for detection of tropical cyclones and atmospheric rivers in gridded atmospheric simulation data

Tim Radke[1], Susanne Fuchs[1], Christian Wilms[3], Iuliia Polkova[2,4,5], and Marc Rautenhaus[1,2]

[1]Visual Data Analysis Group, Universität Hamburg, Hamburg, 20146, Germany

[2]Center for Earth System Research and Sustainability (CEN), Universität Hamburg, Hamburg, 20146, Germany

[3]Computer Vision Group, Universität Hamburg, Hamburg, 22527, Germany

[4] Institute of Oceanography, Universität Hamburg, Hamburg, 20146, Germany

[5] now at Deutscher Wetterdienst, Offenbach am Main, 63067, Germany

Correspondence to: Tim Radke (tim.radke@uni-hamburg.de)

Abstract. Detection of atmospheric features in gridded datasets from numerical simulation models is typically done by means of rule-based algorithms. Recently, the feasibility of learning feature detection tasks using supervised learning with convolutional neural networks (CNNs) has been demonstrated. This approach corresponds to semantic segmentation tasks widely investigated in computer vision. However, while in recent studies the performance of CNNs was shown to be comparable to human experts, CNNs are largely treated as a "black box", and it remains unclear whether they learn the features for physically plausible reasons. Here we build on the recently published "ClimateNet" dataset that contains features of tropical cyclones (TCs) and atmospheric rivers (ARs) as detected by human experts. We adapt the explainable artificial intelligence technique "Layer-wise Relevance Propagation" (LRP) to the semantic segmentation task and investigate which input information CNNs with the Context-Guided Network (CG-Net) and U-Net architectures use for feature detection. We find that both CNNs indeed consider plausible patterns in the input fields of atmospheric variables. For instance, relevant patterns include point-shaped extrema in vertically integrated precipitable water (TMQ) and circular wind motion for TCs. For ARs, relevant patterns include elongated bands of high TMQ and eastward winds. Such results help to build trust in the CNN approach. We also demonstrate application of the approach for finding the most relevant input variables (TMQ is found to be most relevant, while surface pressure is rather irrelevant) and evaluating detection robustness when changing the input domain (a CNN trained on global data can also be used for a regional domain but only partially contained features will likely not be detected). However, LRP in its current form cannot explain shape information used by the CNNs, although our findings suggest that the CNNs make use of both input *values* and the *shape* of patterns in the input fields. Also, care needs to be taken regarding the normalization of input values, as LRP cannot explain the contribution of bias neurons, accounting

for inputs close to zero. These shortcomings need to be addressed by future work to obtain a more complete explanation of CNNs for geoscientific feature detection.

1. Introduction

The automated detection and tracking of 2-D and 3-D atmospheric features including cyclones, fronts, jet streams, or atmospheric rivers (ARs) in simulation and observation data has multiple applications in meteorology. For example, automatically detected features are used for weather forecasting (e.g., Hewson and Titley, 2010; Mittermaier et al., 2016; Hengstebeck et al., 2018), statistical and climatological studies (e.g., Dawe and Austin, 2012, Pena-Ortiz et al., 2013, Schemm et al., 2015, Sprenger et al., 2017, Lawrence and Manney, 2018), and visual data analysis (e.g., Rautenhaus et al., 2018; Bösiger et al., 2022; Beckert et al 2023). Features are typically detected based on a set of physical and mathematical rules. For example, cyclones can be identified by searching for minima or maxima in variables including mean sea level pressure and lower-tropospheric vorticity (Neu et al., 2013; Bourdin et al. 2022). Atmospheric fronts can be identified by means of derivatives of a thermal variable combined with threshold-based filters (Jenkner et al., 2010; Hewson and Titley, 2010; Beckert et al., 2023), and ARs based on thresholding and geometric requirements (Guan and Waliser, 2015; Shields et al., 2018).

Recent research has shown that, given a pre-defined labelled dataset, supervised learning with artificial neural networks (ANNs), in particular convolutional neural networks (CNNs), can learn a feature detection task. For example, Kapp-Schwoerer et al. (2020) and Prabhat et al. (2021) (abbreviated as KS20 and P21 hereafter) showed that CNNs can be trained to detect tropical cyclone (TC) and AR features. Lagerquist et al. (2019), Biard and Kunkel (2019), Niebler et al. (2022), and Justin et al. (2023) used CNNs to detect atmospheric fronts. In these works, CNNs are used to classify individual grid points of a gridded input dataset according to whether they belong to a feature. This corresponds to a “semantic segmentation task” widely investigated in the computer vision literature for segmentation and classification of regions in digital images, e.g., cars, trees, or road surface (Long et al., 2015; Liu et al., 2019; Xie et al., 2021; Manakitsa et al., 2024).

Using CNNs for feature detection via semantic segmentation can have several advantages. These include increased computational performance (Boukabara et al., 2021; Higgins et al., 2023) and the option to learn features that are difficult to formulate as a set of physical rules (P21; Niebler et al., 2022; Tian et al., 2023). A major limiting factor, however, is that they are “black box” algorithms that do not allow for an easy interpretation of the decision-making process inside CNNs. Hence, one does not know whether a CNN bases its decision on plausible patterns in the data. If not, a CNN may still perform well on the training data but fails to generalize to unseen data (Lapuschkin et al., 2019). To approach this issue, the artificial intelligence (AI) community has proposed methods for explainable artificial intelligence (xAI) in the past decade (Linardatos et al., 2021; Holzinger et al., 2022; Mersha et al., 2024). Examples include Layer-wise Relevance Propagation (LRP; Bach et al., 2015), Local Interpretable Model-Agnostic Explanations (LIME; Ribeiro et al., 2016), Gradient-weighted

Class Activation Mapping (Grad-CAM; Selvaraju et al., 2017), and Shapley Additive Explanations (SHAP; Lundberg and Lee, 2017). In short, these methods provide information about what an ANN “looks at” when computing its output, hence allow evaluation of the plausibility of the learned patterns.

The xAI methods vary with respect to several characteristics. For example, the relevance of the input data can be computed per input grid point[1] or for entire regions of the input data, and per input variable[2] or jointly for all variables. Also, the complexity of implementation differs. For application in semantic segmentation, an open challenge is also that existing xAI methods have been mainly developed for classification tasks, i.e., for CNNs assigning input data to one of several classes (this corresponds to the question “is a particular feature contained in the input data” instead of identifying the spatial structure of a feature). While Grad-CAM is readily available for use with semantic segmentation (Captum, 2023; MathWorks, 2023), it has the drawback of not being able to differentiate between input variables (Selvaraju et al., 2017). SHAP can be implemented for semantic segmentation (e.g., Dardouillet et al., 2023), however, it computes relevance values for clusters of input grid points and not for individual input grid points. The same applies to LIME; moreover, to the best of our knowledge, we are not aware of implementations of LIME for semantic segmentation. The feasibility of using LRP for semantic segmentation has been demonstrated in the context of medical imaging (Tjoa et al., 2019; M. A. Ahmed and Ali, 2021) and it produces relevance information per grid point and input variable.

Our goal for the study at hand is to provide an xAI method that works with semantic segmentation CNNs trained to detect atmospheric features. We are interested in opening the “black box” to investigate whether a CNN uses physically plausible input patterns to make its decision. This requires analysis of the spatial distribution of input relevance (i.e., which regions and structures are relevant for a particular feature; hence relevance information *per grid point* is needed), as well as analysis of distributions of relevant input variables (i.e., which values of which input variables are of importance to detect a feature; hence relevance information *per input variable* are needed).

As application example, we consider the work by KS20 and P21, who introduced an expert-labelled dataset of TCs and ARs in atmospheric simulation data (the “ClimateNet” dataset). KS20 and P21 trained two different CNN architectures, DeepLabv3+ (Chen et al., 2018) and Context-Guided Network (CG-Net; Wu et al., 2021), to perform feature detection via semantic segmentation. The studies showed that for the given task, the CNNs learnt to detect TCs and ARs and that the CG-Net architecture outperformed the DeepLabv3+ architecture. However, in neither study an xAI technique was applied.

Mamalakis et al. (2022) (abbreviated as M22 hereafter) recently presented work in this direction by reformulating the P21 segmentation task into a classification task and evaluating several available xAI techniques for classification, including LRP and SHAP. They considered sub-regions of the global dataset used by P21 and differentiated whether zero, one, or more ARs

[1] Computer vision literature concerned with image data uses the term “pixel” for individual input data points. In this study we are concerned with gridded simulation data and hence use the term “grid point”.

[2] Similarly, we use the term “input variable” instead of “colour channel” commonly used in computer vision.

exist in a sub-region. TCs were not considered. M22 showed that for their classification setup, LRP yielded useful information to assess the plausibility of the decision-making inside the CNN. LRP has also been successfully applied in further geoscientific studies concerned with use of CNNs for classification tasks (Beobide-Arsuaga et al., 2023; Davenport and Diffenbaugh, 2021; Labe and Barnes, 2022; Toms et al., 2020). It also fulfils our requirement of computing relevance information per grid point and input variable (at least in some variants; cf. M22).

In this study, we build on the work by KS20, P21, and M22. We demonstrate and analyse the use of LRP for the KS20/P21 case of detecting TCs and ARs, using the CG-Net architecture used by KS20 and the ClimateNet dataset provided by P21 (Sect. 2). We reproduce the KS20/P21 setup (Sect. 3) and address the following objectives:

1. Adapt LRP to the semantic segmentation task for geoscientific datasets and extend the method to be applicable to the CG-Net CNN architecture (Sect. 4).
2. Examine the plausibility of spatial relevance patterns and distributions of relevant inputs for TC and AR detection as computed with LRP (Sects. 5 and 6).
3. Demonstrate further applications of LRP for semantic segmentation, including assessment of the most relevant input variables for a feature detection task and assessment of the robustness of feature detection when data of sub-regions instead of global data is used as input (Sect. 7).

For comparison and due to its widespread use for semantic segmentation in computer vision, we also consider the U-Net architecture (Ronneberger et al., 2015). To limit paper length, however, its results are mainly presented in the Supplement.

2. The ClimateNet dataset

The ClimateNet dataset introduced by P21 contains global 2-D longitude-latitude grids of selected atmospheric variables at a collection of time steps from a simulation conducted with the Community Atmospheric Model (CAM5.1; Wehner et al., 2014), spanning a time interval from 1996 to 2013 (note that this is not reanalysis data). Each grid has a size of 768×1152 grid points and contains 16 variables, listed in Table 1. Experts labelled 219 time steps, assigning each grid point to one of three classes: background (BG), TC, and AR. An individual feature is represented by connected grid points of the same class. As most time steps were labelled by multiple experts, the dataset contains 459 input-output mappings, with sometimes very different labels for the same input data. As P21 argued, these disagreements in classifications reflect the diversity in views and assumptions by different experts. P21 split the labelled data into a training (398 mappings) and test dataset (61 mappings) by taking all time steps prior to 2011 as training data and all other as test data.

Following KS20, we apply z-score normalization on each variable to set the mean values to 0 and the standard deviations to 1, hence achieving equally distributed inputs. As discussed by LeCun et al. (2012), this normalization reduces the convergence time of CNNs during training. Also, z-score normalization helps to treat all input variables equally important by a CNN (e.g., Chase et al., 2022). An issue when using LRP (and other xAI methods; cf. M22) with z-score normalized data, however, is the “ignorant-to-zero-input issue” discussed by M22: zero input values are assigned zero relevance. We will discuss the impact of this issue on the usefulness of the LRP results. For comparison, we also discuss results obtained by training the CNNs using a min-max normalization (which rescales the variable values to the range [0, 1]; e.g., García et al., 2014) and a modified z-score normalization shifted by a value of +10 in the normalised data domain (the mean value becomes +10; the standard deviation remains 1).

Table 1: Atmospheric 2-D fields (variables) contained in the P21 ClimateNet dataset. Variable short names are used throughout the text.

Variable	Description	Mean	Standard Dev.	Units
U850	Zonal wind at 850 mbar pressure surface	1.56	8.29	m/s
V850	Meridional wind at 850 mbar pressure surface	0.270	6.22	m/s
UBOT	Lowest level zonal wind	0.129	6.65	m/s
VBOT	Lowest model level meridional wind	0.332	5.77	m/s
TS	Surface temperature (radiative)	271	23.7	K
T200	Temperature at 200 mbar pressure surface	213	7.99	K
T500	Temperature at 500 mbar pressure surface	253	12.8	K
TREFHT	Reference height temperature	279	22.5	K
TMQ	Total (vertically integrated) precipitable water	19.3	15.8	kg/m^2
QREFHT	Reference height humidity	7.83 x 10^{-3}	6.20 x 10^{-3}	kg/kg
PRECT	Total (convective and large-scale) precipitation rate (liq + ice)	2.95 x 10^{-8}	1.56 x 10^{-7}	m/s
ZBOT	Lowest model level height	61.3	4.91	m
Z200	Geopotential Z at 200 mbar pressure surface	11.7 x 10^{3}	0.635 x 10^{3}	m
Z1000	Geopotential Z at 1000 mbar pressure surface	474	833	m
PS	Surface pressure	96.6 x 10^{3}	9.71 x 10^{3}	Pa
PSL	Sea level pressure	101 x 10^{3}	1.46 x 10^{3}	Pa

3. Reproduction of the KS20/P21 task with CG-Net and U-Net

Following KS20/P21, we formulate the detection of TCs and ARs as a semantic segmentation task, with the goal of assigning one of the classes TC, AR, or BG to every grid point. We evaluate the CG-Net (Wu et al., 2021; shown by KS20 to outperform the DeepLabv3+ architecture used by P21) and U-Net (Ronneberger et al., 2015) CNN architectures. Figure 1 illustrates both architectures. CNNs are a class of ANNs that capture spatial patterns by successively convolving the data with spatially local kernels (e.g., Russell and Norvig, 2021). For semantic segmentation tasks, CNNs compute as output a probability value for each grid point and class. U-Net features an encoder-decoder architecture that first successively decreases the grid size to detect high-level patterns at different scales using convolutional layers, followed by upsampling and a combination of the extracted patterns leading to segmentation as output. To improve the quality of the segmentation, skip connections between the respective levels of the encoder and decoder are introduced. In contrast, CG-Net uses a typical classification-style CNN architecture (Simonyan and Zisserman, 2015) without a dedicated decoder. It uses context guided blocks that combine spatially local patterns with larger-scale patterns to produce a final segmentation.

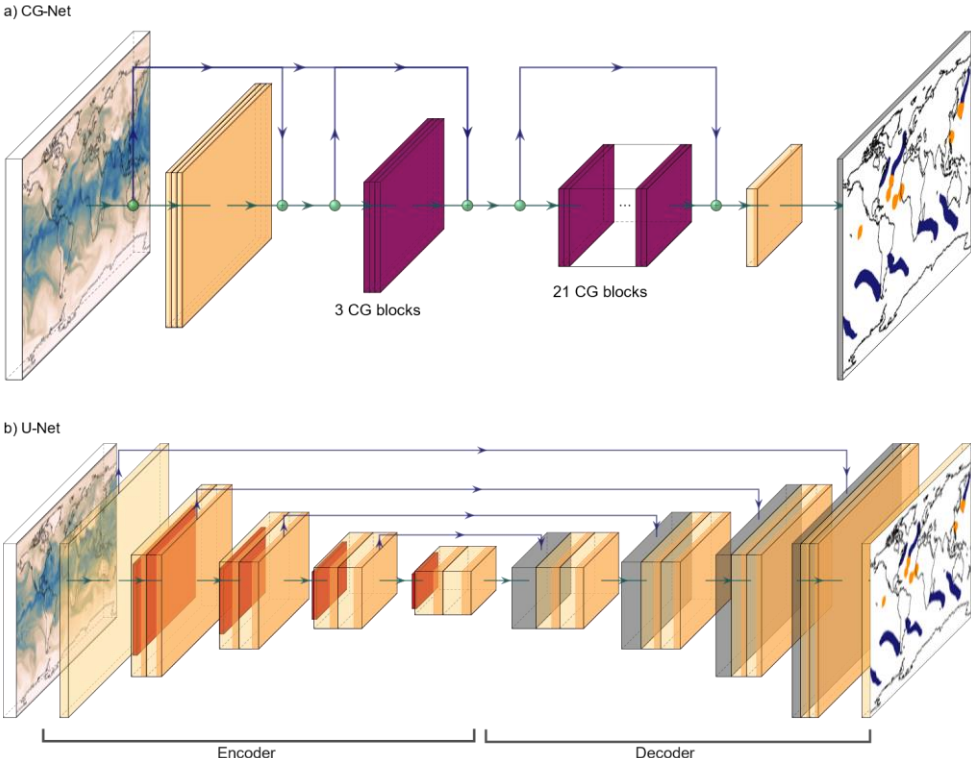

Figure 1: Schematic illustration of the (a) CG-Net (Wu et al., 2021) and (b) U-Net (Ronneberger et al., 2015) CNN architectures. Yellow colour denotes convolutional layers, red average pooling layers, blue/grey transposed convolutional layers, violet context guided blocks. Blue arrows indicate skip connections.

We use the same CG-Net configuration used by KS20, who in turn followed Wu et al. (2021). Our U-Net configuration is based on Ronneberger et al. (2015). For training CG-Net and U-Net, we follow KS20. Most grid points in the ClimateNet dataset belong to the background class, hence an imbalance exists between the frequency of the three classes. KS20 use the Jaccard loss function beneficial in cases of class imbalance (Rahman and Wang, 2016). It applies the Intersection over Union

(IoU; Everingham et al., 2010) metric commonly used in semantic segmentation (e.g., Cordts et al., 2016; Zhou et al., 2017; Abu Alhaija et al., 2018). The IoU score characterizes the overlap of two features by dividing the size (in the computer vision literature as number of pixels, in our case in grid points) of feature intersection by the size of feature union[3]. If two features are identical, the IoU score equals 1, if they do not overlap at all, the score equals 0. The Jaccard loss function is minimized (equivalent to maximising IoU) using the Adam optimizer (Kingma and Ba, 2014), with a learning rate of 0.001. Since random weight initialization leads to differing results in different training runs (Narkhede et al., 2022), we train each network five times and select the best performing. We use convolution kernels of size 3x3 grid points. Grid boundaries in longitudinal direction are handled with circular (i.e., cyclic) padding; at the poles, replicate padding is used.

KS20 as well as P21 use only a subset of the 16 variables contained in the ClimateNet dataset: TMQ, U850, V850, and PSL in KS20, and TMQ, U850, V850, and PRECT in P21. We reproduce the KS20 CG-Net setup for our objective of investigating whether it bases its detection on plausible patterns. For evaluation, IoU scores are computed for each feature class individually and for comparison with values provided by KS20 as multiclass means. All scores are computed for the test data (cf. Sect. 2) and listed in percent.

Table 2: Intersection over union scores reached by CG-Net trained as proposed by KS20, using a batch size of 4 and 10. For comparison, scores for U-Net are provided. All values are computed for the test data and are listed in percentages. The highest score per column is written in bold.

CNN implementation	AR	TC	AR-TC Mean	BG	AR-TC-BG Mean
CG-Net implementation by KS20, batch size 4	**40.8**	35.3	38.0	94.1	56.7
CG-Net implementation by KS20, batch size 10	40.3	35.9	**38.1**	94.4	56.8
U-Net (Ronneberger et al., 2015), batch size 4	40.2	36.0	**38.1**	94.3	56.8
U-Net with num. of neurons per layer reduced to ¼ of Ronneberger et al. (2015), batch size 10	40.1	**36.1**	**38.1**	**94.7**	**57.0**

Table 2 lists evaluation results for both CG-Net and U-Net. KS20 only provide an evaluation score for the AR-TC-BG mean of 56.1%. Our reproduction (using the same implementation) yields a similar score (slightly different due to random initialization); Table 2 in addition shows the scores for the individual feature classes. KS20 use a training batch size of 4; with 20 training-evaluation epochs a single training run takes about 19 min on an 18-core Intel Xeon® Gold 6238R CPU with 128 GB RAM and a Nvidia A6000 GPU with 48 GB VRAM. To speed up training, the batch size can be increased. For

[3] Note that this approach does not entirely correspond to the geometric area of the features on the globe. For features that occur closer to the poles a metric based on the geometric feature area would be more suitable.

instance, a batch size of 10 reduces training time for a single run by 10% without significantly deviating from the evaluation results. The U-Net implementation achieves similar scores, confirming that the detection task can be learned by different CNN architectures. Also, our experiments showed that for U-Net, reducing the number of neurons per layer to one quarter compared to the original Ronneberger et al. (2015) implementation reduces training time by 35% without significantly deviating from the evaluation results. One may hypothesize that due to its larger number of weights the U-Net architecture has an increased potential to learn complex tasks and thus may achieve higher IoU scores for the problem at hand. This, however, seems not to be the case. Also, U-Net in our case requires 50 training-evaluation epochs to converge, requiring about 46 min on our system.

Concluding, all CNN setups achieve very similar evaluation scores, which provides confidence that they are learning similar structures that can be further analysed using LRP.

We note that the size of the ClimateNet dataset (cf. Sect. 2) can be considered small for training a deep CNN, a challenge also encountered, e.g., in the literature for medical image segmentation (e.g., Rueckert and Schnabel, 2020; Avberšek and Repovš, 2022). P21 stated they expect CNN performance to improve if a larger dataset was available. However, we also note that ClimateNet's characteristics of containing differing labels by multiple experts for many time steps may be effective in avoiding overfitting. Also, it may limit achievable IoU scores. If strong overfitting was present, we expect physically implausible structures to show up in the LRP results. Also, strong overfitting typically results in evaluation scores being distinctly better for the training data compared to the test data (e.g., Bishop, 2007). For example, for the CG-Net implementation by KS20, batch size 10, we obtain the following IoU scores for the training data: AR = 43.6%, TC = 37.7%, BG = 95.2%, AR-TC-BG mean = 58.8%. These scores are very close to those listed in Table 2 for the test data, indicating that no overfitting is present. In comparison, if we deliberately overfit CG-Net by training with 100 training-evaluation epochs (instead of 20), we obtain IoU scores of AR = 60.0%, TC = 53.3%, BG = 96.7%, AR-TC-BG mean = 70.0% for the training data and AR = 37.8%, TC = 32.5%, BG = 94.4%, AR-TC-BG mean = 55.0% for the test data.

4. Adapting LRP to semantic segmentation

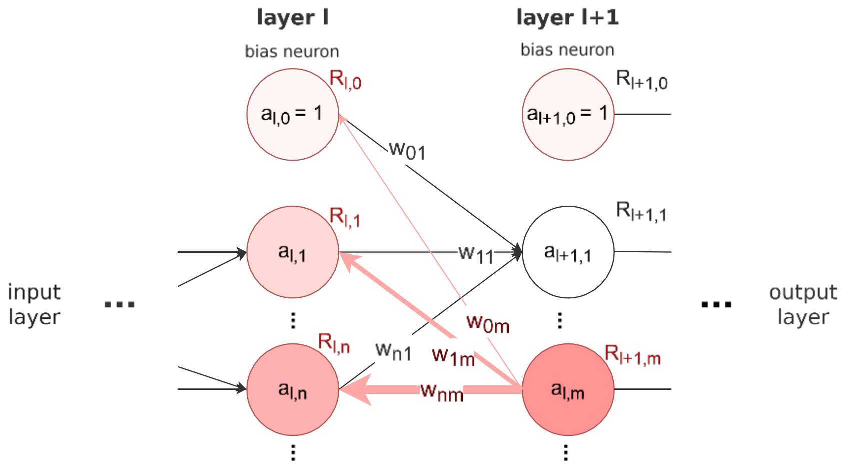

Figure 2: Schematic illustration of two (hidden) layers of an ANN (cf. Eq. 1). *$a_{l,m}$* denotes the activation of neuron *m* in layer *l*, *$R_{l,m}$* the corresponding relevance, *$w_{n,m}$* the weight between neuron *n* and *m*. Neuron "0" of each layer is a bias neuron. Red colour intensity symbolises exemplary relevance backpropagated from neuron *m* in layer *l+1* towards layer *l*, distributed according to neuron activation and weights. In setups discussed in this study, activation *a* and relevance *R* are 3-D grids with size of the current layer-dependent horizontal grid times the number of classes; the weights *w* can be scalars or convolution kernels depending on layer type.

For our first objective, we adapt LRP to the semantic segmentation task. LRP was originally developed to understand the decision-making process of ANNs designed for solving classification tasks (Bach et al., 2015). After a classification-ANN has computed class probabilities from some input data grid, LRP considers a single feature class by only retaining its probability (all other class probabilities are set to zero). This modified output is interpreted as initial value for the relevance to be computed; it is propagated backwards through the network towards the input layer. Figure 2 illustrates the approach. In an iterative process, the relevance $R_{l+1,m}$ of a given neuron *m* in a network layer $l + 1$ is distributed over all neurons *n* in the preceding layer *l* (conserving the total relevance). Practically, this is implemented by iteratively computing the relevance $R_{l,n}$ of the neurons in layer l, as proposed by Montavon et al. (2019):

$$\mathbf{R_{l,n}} = \sum\nolimits_{\mathbf{m}} \frac{\mathbf{a_{l,n}} \cdot \boldsymbol{\rho}\left(\mathbf{w_{l,n}^{(l+1),m}}\right)}{\boldsymbol{\epsilon} + \sum_{n} \mathbf{a_{l,n}} \cdot \boldsymbol{\rho}\left(\mathbf{w_{l,n}^{(l+1),m}}\right)} \mathbf{R_{l+1,m}} \qquad \textbf{(1)}$$

Here, $a_{l,n}$ denotes the activation value of neuron n, $\mathrm{w}_{\mathrm{l,n}}^{(\mathrm{l+1}),\mathrm{m}}$ the weights between neurons n and m, ρ an optional function that modulates the weights, and ϵ a constant value that can be used to absorb weak or contradictory relevance. Note that in our case, activation a and relevance R are 3-D grids. Their size is given by the size of the 2-D data grid of the respective layer, times the number of classes. The weights w can be scalars or convolution kernels depending on layer type. We refer to Montavon et al. (2019) for further details. In this study, we use the so-called LRP$_z$ rule (M22; also called LRP-0 rule; e.g., Montavon et al., 2019). That is, the function ρ is a simple identity mapping, and ϵ equals $1 \cdot 10^{-9}$ to prevent division by zero. The relevance distribution of the input layer is the desired result. LRP$_z$ distinguishes between positive and negative contributions. They can be interpreted as arguments *for* (positive relevance) and *against* (negative relevance) classifying grid points as belonging to a feature.

Other LRP rules exist, M22 discussed their properties for CNN architectures designed for classification (note that the LRP$_{comp}$ and LRP$_{comp/flat}$ rules recommended by M22 are not directly applicable to our setup; e.g., our CNNs do not contain fully connected layers; also, the LRP$_{comp/flat}$ rule cannot distinguish between different input variables).

As noted in Sect. 2, LRP using the LRP$_z$ rule suffers from what is by M22 referred to as the “ignorant-to-zero-input issue”. An ANN’s bias neurons (e.g., Bishop, 2007; index 0 in each layer in Figure 2) are required, e.g., to consider input values close to zero that would otherwise have no effect on the ANN output due to the multiplicative operations at each neuron (e.g., Saitoh, 2021). Due to the design of LRP$_z$, relevance assigned to bias neurons is not passed on to the previous layer and will not be included in the final result. Hence, input values of zero will receive zero relevance (Montavon et al., 2019).

For our setup we note that, in contrast to the ANNs used by M22, CG-Net and U-Net as used in the present study contain batch normalization layers (Ioffe and Szegedy, 2015). These layers apply z-score normalization to the output of the convolutional layers. Additionally, the normalized values are shifted and rescaled according to two learned parameters β and γ. This normalization cancels the bias effect. It is, however, subsumed by β and still present. In practical implementations, the bias neurons and weights are hence deactivated during training (Ioffe and Szegedy, 2015). This becomes relevant for the computation of relevance, which can be done separately for convolutional layers (Bach et al., 2015) and batch normalization layers (Hui and Binder, 2019). Alternatively, implementations have been proposed in which both layers are merged, with the advantage that relevance needs to be computed only for the merged layer (Guillemot et al., 2020). In our work, relevance needs to be computed many times for a given ANN (for grid points and features). For efficiency we choose the second option, as a merged layer needs to be computed only once. The merged layer weights are inferred from the original two layers. In particular, the bias weights are reintroduced, and the ignorant-to-zero-issue persists as in M22.

LRP implementations for classification tasks have been described in the literature (e.g., Montavon et al., 2019; M22). For semantic segmentation tasks, the question arises how the gridded output (instead of single class probabilities) should be considered. A straightforward approach is to consider an individual detected feature (i.e., a region of connected grid points of the same class) and to compute a relevance map for each grid point of the feature, i.e., treating each grid point as an individual classification task. Then, the resulting relevance maps can be summed to obtain a total feature relevance. While for a given location the contribution from different relevance maps can be of opposite sign, the sum expresses the predominant signal. For more detailed analysis, positive and negative relevance can be split into separate maps. Also, we propose to compute the extent to which different grid points of a feature contribute to the (total or positive or negative) relevance in a selected region R. The resulting maps show, for each grid point of a feature, the summed relevance that this point has contributed to all grid points in R.

An important aspect is that the absolute relevance values computed by LRP depend on the absolute probability values computed by the CNN. For example, if a grid point is classified as TC based on probabilities (TC=0.3, AR=0.2, BG=0.1), the corresponding relevance map will contain lower absolute relevance values than if the probabilities were, e.g., (TC=0.8, AR=0.6, BG=0.4). The question arises whether the relevance values should be normalized before summation, as the absolute probability values are not relevant for assigning a grid point to a particular class. They can, however, be interpreted as how "likely" the CNN is in assigning a class to a certain grid point. This aligns with Montavon et al. (2019), who link the ANN output with the probability of each predicted class. We hence argue that for all grid points belonging to a given feature, no normalization should be applied. This way, in the resulting total relevance map the individual grid points' contributions are weighted according to their probability of belonging to the feature, higher relevance is deemed to be more important for the overall feature as well.

To compare relevance maps of distinct features, or to jointly display the relevance of multiple features in a single map, we however argue that the relevance maps of the individual features should be normalized first. This ensures that the spatial structures relevant for the detection of a feature show up at similar relevance magnitudes.

For computing relevance maps for the individual grid points an existing LRP implementation for classification, e.g. Captum (Kokhlikyan et al., 2020), can be used by adding an additional layer to the network that reduces the output grid to a single point (this corresponds to setting the output probabilities of all grid points except the considered one to zero). This approach has recently been used by Farokhmanesh et al. (2023) for an image-to-image task similar to semantic segmentation. The resulting relevance maps can in a subsequent step be summed and normalized. Depending on grid size and number of neurons in the CNN, this approach, however, can be time-consuming (in our setup, a single LRP pass requires about 100 ms; with an AR feature typically consisting of more than 5000 grid points in the given dataset, calculating LRP with this approach sums to about 8 min for an AR feature). To speed up the computation, we modify the approach by retaining the output probabilities of all grid points that belong to a specific feature. The LRP algorithm is executed only once (thus only requiring about 100 ms for an entire AR feature). Due to the distributive law for addition and multiplication, this is equivalent to the first approach. This approach has also been used by Ahmed and Ali (2021) for a specific U-Net architecture in a medical application, although for the entire data domain instead of individual features.

To apply LRP with the CG-Net architecture, the additional challenge of handling CG-Net-specific layer types arises. In addition to layer types also present in the U-Net architecture (for which LRP implementations have been described in the literature, including convolutional layers, Montavon et al., 2019; pooling layers, Montavon et al., 2019; batch normalization layers, Hui and Binder, 2019; Guillemot et al., 2020; and concatenation-based skip connections, Ahmed and Ali, 2021), CG-Net uses addition-based skip connections, a spatial upscaling layer, and a global context extractor (GCE; Wu et al., 2021).

For addition-based skip connections, we first calculate the relative activations of both the skip connection and the direct connection in relation to the summed activation. Next, the relevance of the subsequent deeper layer is multiplied with these relative activations to determine the relevance for both connections. LRP for spatial upscaling layers is calculated by spatially downscaling the relevance maps by the corresponding scaling factor. Following the argumentation by Arras et al. (2017) for adapting LRP to multiplicative gates in Long Short-Term Memory (LSTM) units, we omit the relevance calculation of GCE units.

5. Case study: Plausibility of spatial relevance patterns for detected TC and AR features

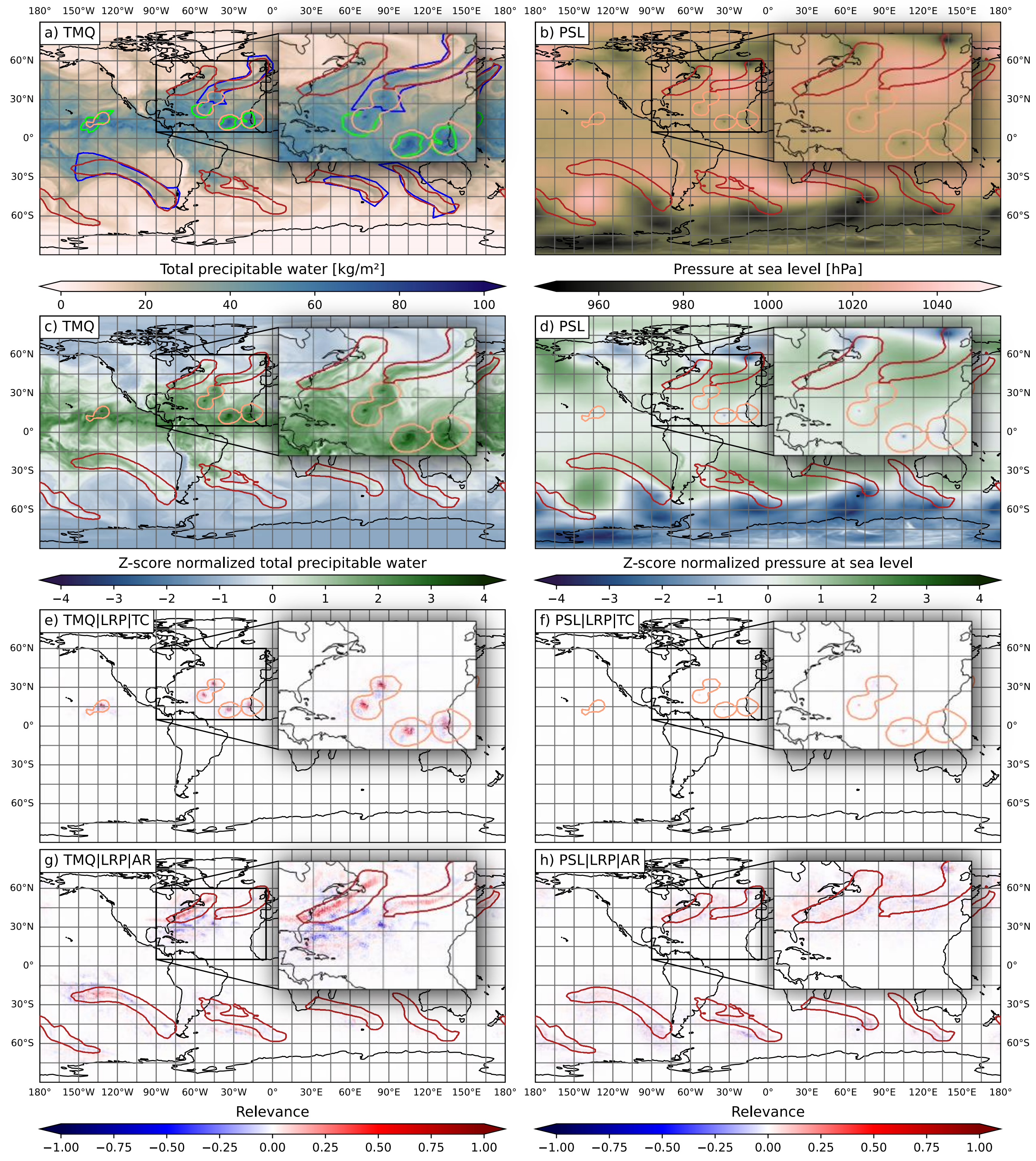

Figure 3: Global maps of (a) TMQ and (b) PSL for the time step contained for 27 September 2013 in the ClimateNet dataset. Orange (red) contours show TC (AR) features detected with CG-Net using the KS20 setup. Green (blue) contours show TC (AR) features labelled by an expert. Panels (c) and (d) show z-score normalized fields input to the ANN. Panels (e) and (f) show summed TMQ and PSL relevance of all grid points classified as TC, panels (g) and (f) the summed relevance of all grid points classified as AR.

For our second objective, we discuss the example of the time step labelled “27 September 2013”. We assess the plausibility of spatial relevance patterns obtained using our adapted LRP approach and the CG-Net setup that reproduces the KS20 setup (using z-score normalization; cf. Table 2). In the chosen example, several TC and AR features were present that we consider representative.

Figure 3a/b shows global maps of TMQ and PSL of the chosen time step, overlaid with expert-labelled and CNN-detected TC and AR features. Distinct features in the North Atlantic region are enlarged. In general, TCs are characterized by high humidity and minima in PSL (e.g., Stull, 2017), ARs by strong horizontal moisture transport (implying high humidity and wind speed; e.g., Ahrens et al., 2012). ARs also take the form of elongated bands of elevated humidity connected to mid-latitude cyclones (Gimeno et al., 2014). These aspects are commonly used by rule-based detection methods (e.g., Tory et al., 2013; Shields et al., 2018; Nellikkattil et al., 2023), we are hence interested in whether CG-Net learns similar aspects.

In addition, Fig. 3c/d shows the z-score-normalized TMQ and PSL fields that are the actual input to the ANN. As discussed in Sect. 4, the employed LRP$_z$ rule is “ignorant to zero input” (M22), it is hence important to see where zero values are input to the CNN.

Figure 3e/f shows the relevance of TMQ and PSL for the detected TC features (i.e., the summed relevance of all grid points classified as TC as described in Sect. 4). We interpret the relevance maps as “what the CNN looks at” to detect a feature, and where it collects arguments *for* (positive relevance) and *against* (negative relevance) classifying grid points as belonging to a feature. If the relevance is close to zero *despite having a non-zero input value*, the corresponding location is considered irrelevant to the current feature of interest.

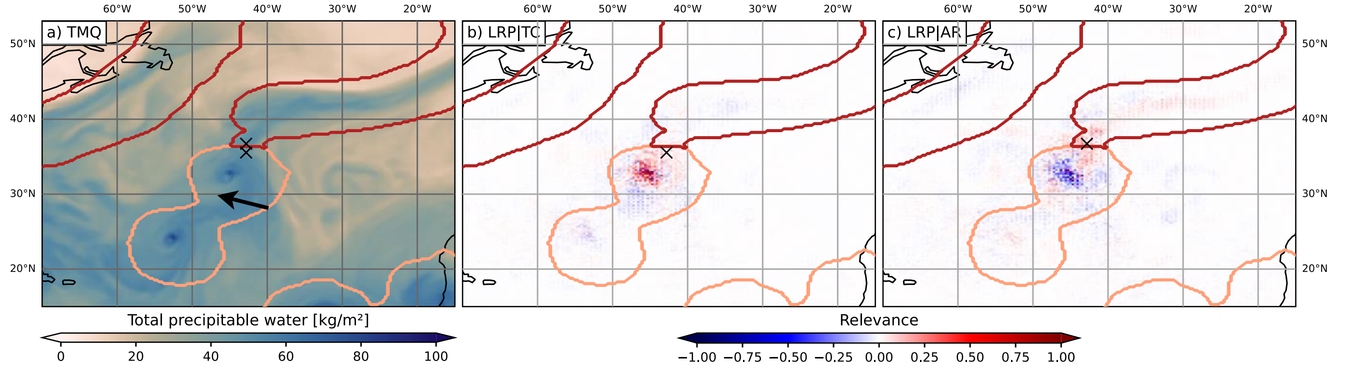

Figure 4: (a) Close-up of TMQ as shown in Fig. 3a for the North Atlantic region. Black "x" mark two selected single grid points, the southern one within the TC feature, the northern one within the AR. (b) TMQ relevance for the southern (TC) grid point. (c) TMQ relevance for the northern (AR) grid point.

For both TMQ and PSL, CG-Net learns to positively consider extreme values at the centre of the detected TCs, with TMQ considered more relevant than PSL (normalized relevance of up to 1.0 vs. up to 0.5). The relevance mostly is spatially confined to the feature region. Positive TMQ relevance is mostly found at TMQ maxima, which also correspond to z-score normalized maxima (Fig. 3a/c). PSL relevance is also collocated with PSL minima, which, however, are surrounded by bands of close-to-zero values after z-score normalization. We hypothesize that this can cause the lower relevance values compared to TMQ. That is, CG-Net could consider PSL values more strongly, but this is not discernible in the LRP$_z$-computed relevance of the used setup.

A further noticeable characteristic in Fig. 3e/f is that the detected TC features are markedly larger than the relevant regions. Here our hypothesis is that CG-Net learnt to classify grid points at a certain distance around point-like extrema as TC. That is, for grid points at the edge of a feature, the most relevant information is that it is at a specific distance to the TMQ maximum and PSL minimum. This hypothesis would be consistent with the specific capabilities of CNNs; their convolution filters take neighbouring grid points into account (e.g., Bishop, 2007). If CG-Net had primarily learned some sort of thresholding on TMQ or PSL, and no information about the spatial structure of the fields, we would have expected the relevance to cover the feature area (with values above/below a specific threshold) more uniformly.

To test the hypothesis, we consider two individual grid points in the inset region in Fig. 3 that are of interest because they are close to the border of the TC and AR features around 45° W and 35° N: How does CG-Net distinguish between the two feature classes in this region? Figure 4 shows TMQ relevance maps for the two points, the southern one being classified as belonging to the TC, the northern one as belonging to the AR (black crosses in Fig. 4a, note that in Fig. 4b/c the relevance for the classification of the single grid points only is shown, not the summed relevance of all feature grid points as in Fig. 3). For the TC grid point, Fig. 4b shows that the CNN considers the nearby TMQ maximum at 43° W and 31° N as a strong argument *for* its decision to classify the point as TC, confirming our hypothesis. Some patches, in particular south of the TC centre, are considered as arguments *against*, though at much weaker relevance magnitude. We hypothesize that this may be due to the shape of the TMQ field in this region with weak filaments of TMQ being drawn into the TC from south-west (arrow in Fig. 4a). We will come back to this issue in the next section. For the AR grid point, CG-Net considers the nearby TMQ maximum as a strong argument against classifying the point as AR. In contrast, the also nearby band of high TMQ extending from 40° W and 40° N towards north-east is considered as an argument for the point being part of an AR. We interpret these findings such that the CNN indeed considers the spatial distance to a point-like TMQ maximum, and possibly also the filamentary structures in TMQ. Note that the final classification decision, however, is of course based on all input fields.

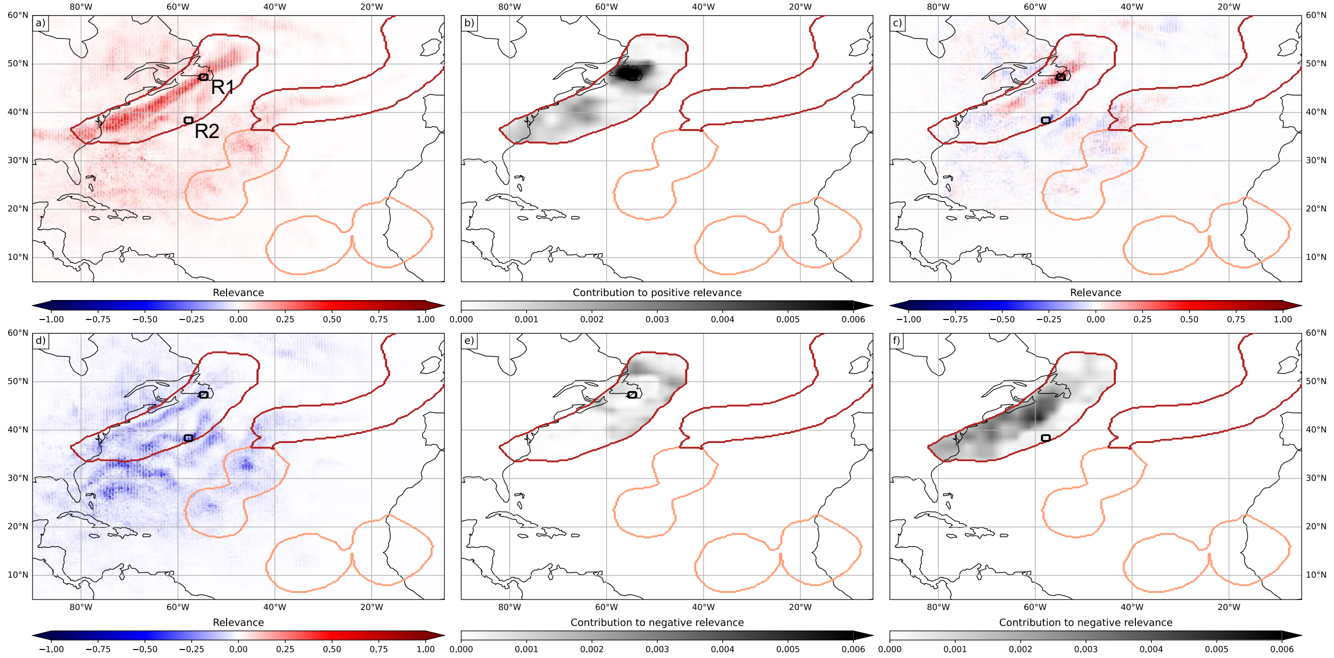

Figure 5: Same as the inset in Fig. 3g but showing (a) only the positive component of total TMQ relevance, (b) parts of the AR that contributed to positive TMQ relevance in region R1, (c) TMQ relevance for classifying the grid point marked with X as AR, (d) only the negative component of total TMQ relevance, (e) parts of the AR that contributed to negative TMQ relevance in R1, (f) the same as (e) but for R2.

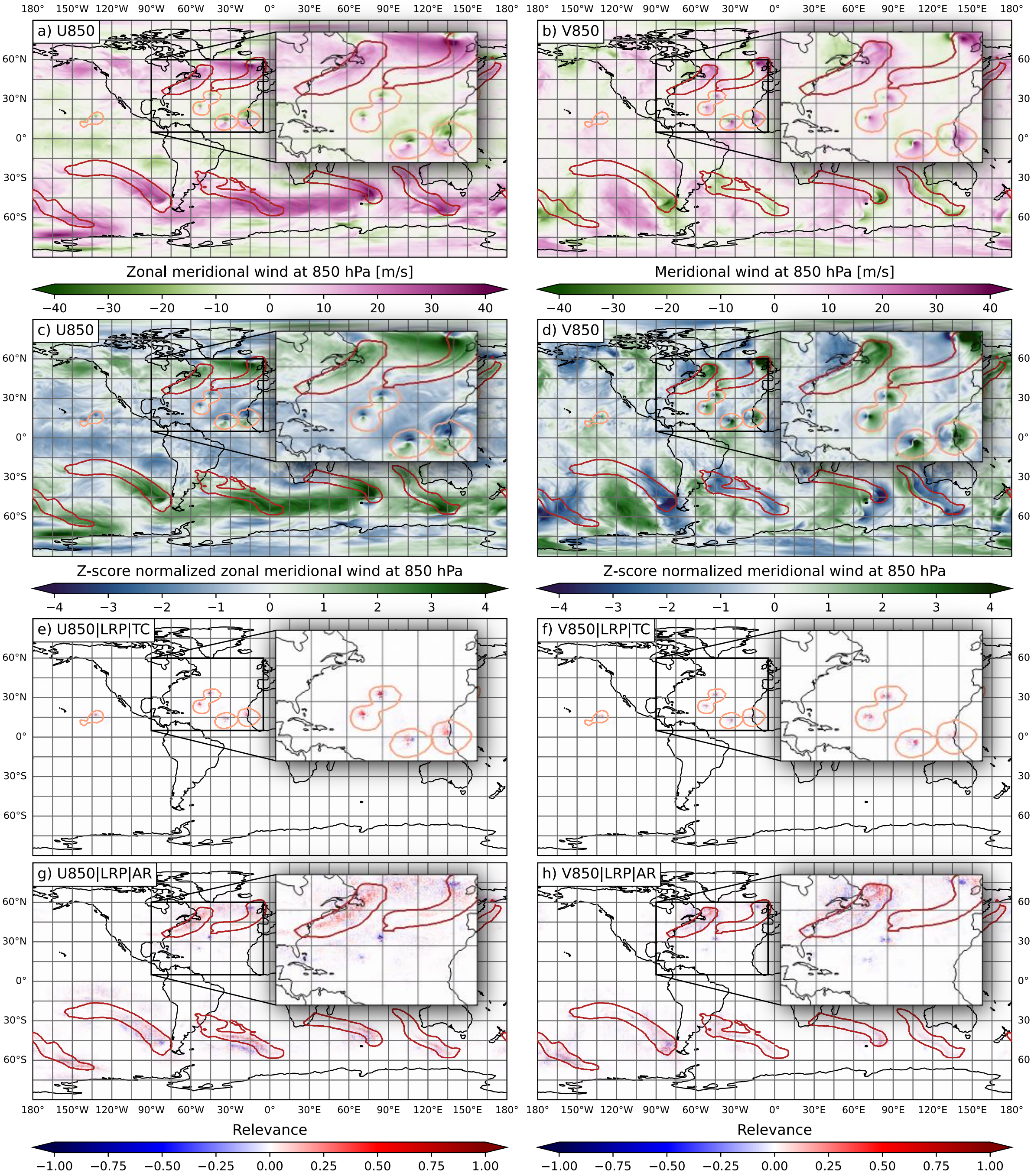
a) U850
b) V850
c) U850
d) V850
e) U850|LRP|TC
f) V850|LRP|TC
g) U850|LRP|AR
h) V850|LRP|AR
180° 150°W 120°W 90°W 60°W 30°W 0° 30°E 60°E 90°E 120°E 150°E 180°
60°N
30°N
0°
30°S
60°S
Zonal meridional wind at 850 hPa [m/s]
Meridional wind at 850 hPa [m/s]
−40 −30 −20 −10 0 10 20 30 40
Z-score normalized zonal meridional wind at 850 hPa
Z-score normalized meridional wind at 850 hPa
−4 −3 −2 −1 0 1 2 3 4
Relevance
−1.00 −0.75 −0.50 −0.25 0.00 0.25 0.50 0.75 1.00

Figure 6: Same as Fig. 3 but for (left column) zonal wind at 850 hPa and (right column) meridional wind at 850 hPa.

Figure 3g/h shows the relevance of TMQ and PSL for the detected AR features. We again focus on the North Atlantic region in the inset, containing two ARs. The elongated band of high TMQ associated with the eastern AR is surrounded by dryer air, making it distinctly stand out in Fig. 3a. CG-Net finds positive relevance in this band, few arguments against the structure being an AR are found in its surroundings except for the discussed TMQ maximum in the TC directly south of the AR (Fig. 3g). However, again we note that if information directly around the band of high TMQ was considered by the CNN, it would not show up in the relevance map as the z-score-normalized values surrounding the band are close to zero (Fig. 3c).

The western AR, however, is not as clearly surrounded by drier air and hence not as clearly discernible in the TMQ field (Fig. 3a). While for this feature also the elongated band of high humidity is taken as an argument for the AR class, at the southern edge and south of the AR regions of arguments against show up (Fig. 3g). We interpret this as some sort of uncertainty of the CNN, like a human expert that would analyse the region around this AR more carefully, also considering other available variables to make their decision.

The western AR also is interesting as it is not among the expert labels (Fig. 3a), although we note that the discussed time step has been labelled by a single expert only (cf. Sect. 2). Is this a “false positive” or did the expert miss a potential AR? To further understand CG-Net’s reasoning, we split the total TMQ relevance into positive and negative components. Also, for selected regions, we investigate which parts of the AR contributed to the relevance (cf. Sect. 4).

Figure 5a shows that for some of the grid points that comprise the AR, the regions of high TMQ at the southern edge and south of the AR are also taken as (weak) arguments for belonging to the AR. Figure 5d shows that for some grid points the elongated band of high TMQ inside the AR is taken as argument against. Further analysis shows that the predominantly positive relevance along the elongated band is mostly caused by grid points on or close to the band. As an example, Fig. 5b shows that positive relevance in a selected region R1 is mostly caused by grid points inside and around R1. Individually, these grid points show relevance patterns as shown in Fig. 5c. Here, with respect to TMQ, the elongated band is the main argument for belonging to the AR. Figure 5e shows that negative relevance in R1 is mostly caused by grid points at a certain distance to R1, with a distinct “blocky” shape that we attribute to the CNN’s convolutional layers. We interpret this as CG-Net having learnt that (1) grid points located on or close to an elongated band of high TMQ likely belong to an AR, and (2) grid points located at some distance to such a structure likely do *not* belong to an AR. Figure 5f confirms this hypothesis. R2 is located on another filament of high TMQ close to but separate from the AR’s “main band” of high TMQ. Negative relevance in R2 is mostly caused by grid points on the AR’s “main band”. For these grid points, being close to another band-like structure of high TMQ seems to be an argument against belonging to an AR.

We provide a more complete picture in Figs. S6 and S7 in the Supplement, showing relevance contribution for further regions. For many grid points in the discussed feature, the presence of the band-like structures of high TMQ at the southern edge and south of the AR counter the arguments of the “main band” for an AR and hence cause “uncertainty”. We argue, however, that this behaviour of the CNN is plausible and that a human expert could also have labelled the structure as an AR.

Figure 3h shows that for AR detection CG-Net cannot infer much information from the PSL field. While it “looked” at the regions surrounding the ARs, the relevance field is weak and noisy, and no recognizable structure is found. This is plausible since in Fig. 3b there are no discernible PSL structures visible for the AR features. To the best of our knowledge, there are also no rule-based systems that use PSL for AR detection.

Figure 6 shows, however, that both 850 hPa wind components are used for the detection of both TCs and ARs. The western AR in the inset is characterized by high zonal wind (Fig. 6a). It coincides with a clearly positively relevant structure (Fig. 6g). Meridional winds are strongest around the mid-latitude cyclone at the northern end of the AR (Fig. 6b). CG-Net also considers this as positively relevant (Fig. 6h). The dipole structure discernible in both wind components close to cyclone centres (both tropical and mid-latitude) is considered as an argument against ARs by the CNN (negative relevance in Fig. 6g/h). Our interpretation is that CG-Net learnt to identify such dipoles with TCs and cannot infer that a mid-latitude dipole north-east of an AR would be an argument for the AR feature. This is supported by that for detection of TC features, the dipoles are considered positively relevant (Fig. 6e/f). Both wind components are also widely used in rule-based detection systems, for example by three of the four algorithms discussed by Bourdin et al. (2022) for detection of TCs. For rule-based AR detection, wind components are contained in the integrated vapor transport (IVT) variable that is commonly used (Shields et al., 2018; Wick et al., 2013).

We conclude the discussion with the interpretation that CG-Net in the present setup learnt overall very plausible structures to detect TCs and ARs, which is very promising for gaining confidence in CNN-based detection of atmospheric features.

Reproductions of Figs. 3 and 6 when using U-Net instead of CG-Net are provided in the Supplement (Figs. S8 and S9). Despite the differences in CNN architecture (cf. Sect. 3), very similar results are found. Notable differences include that the U-Net setup detects smoother feature contours, and that its relevance values are more pronounced and show smoother spatial patterns. We consider it promising, however, that two different CNN architectures learn very similar patterns.

6. Relevant input variable values: The issues of shape and input normalization for explaining feature detection

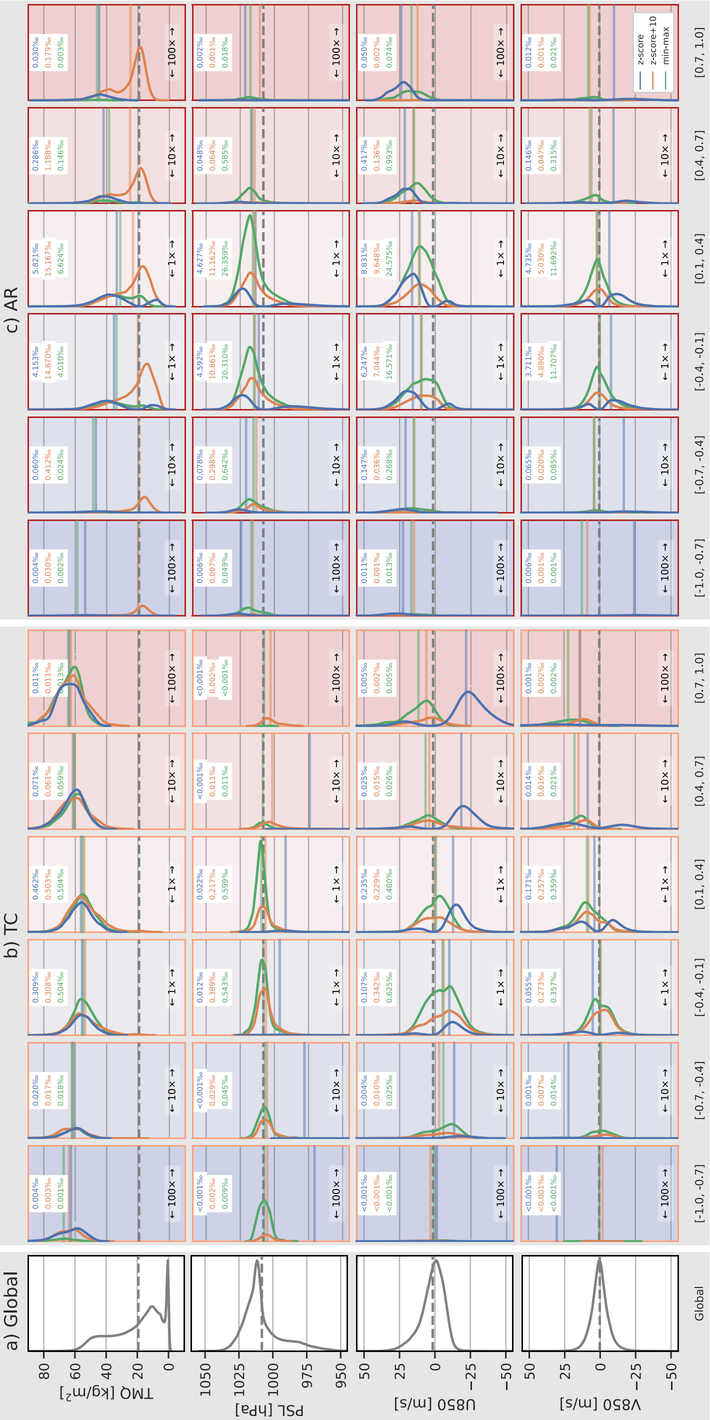

Figure 7: Distributions of CG-Net input variable values in the test dataset. (a) Global distribution (all grid points). Dashed horizontal lines show distribution means, for reference also shown in the other panels. (b) Distributions of grid points with relevance magnitude > 0.1 for TC detection, at six different relevance ranges. The range [-0.1..0.1] is omitted. Shown are distributions for z-score-normalized input values (blue curves), shifted z-score-normalization (orange), and min-max-normalization (green). Horizontal lines show distribution means. The numbers at the top of each box denote fraction (in ‰) of grid points in the corresponding relevance range. Note the horizontal scaling: Since much fewer grid points are assigned high relevance values, to see the shape of the distributions we horizontally scale the relevance range [0.4..0.7] 10 times and the range [0.7..1.0] 100 times compared to the range [0.1..0.4]. (c) Same as (b) but for AR detection.

Figures 3 to 6 showed a single time step that we consider representative as an example of the spatial relevance patterns obtained from LRP. For a more complete picture of what the CG-Net has learnt, we are interested in statistical summaries of input values that it considers relevant. The goal is to see if, for example, also on average high values of TMQ are learnt to be most relevant for TC and AR detection.

We compute distributions over all time steps in the test dataset (cf. Sect. 2) of the CNN input variables, both at all grid points and at grid points considered relevant to different extent (note that, as seen in Figs. 3 and 6, this includes grid points outside the detected features). Figure 7 shows the distributions of TMQ, PSL, U850, and V850. As reference, the value distributions for the entire globe, i.e., all grid points, are shown (Fig. 7a). To learn which variable values are considered relevant by LRP for TC and AR detection, we divide the relevance range [-1..1] into six distinct intervals of width 0.3 and show distributions for each feature and interval. The relevance range [-0.1..0.1] is omitted to mask out regions of zero and low relevance. Note that for all variables, this includes over 98% of all grid points. That is, on average less than 1% of all grid points are assigned relevance values with magnitude larger than 0.1 in the present CG-Net setup. Distributions of the relevance range [-0.1..0.1] hence look very similar to the reference distributions of the entire globe.

First notice that CG-Net for TC detection, also averaged over the entire test dataset, considers high values of TMQ positively relevant. Already for the relevance range [0.1..0.4], the distribution peaks at values slightly above 55 kg m^{-2}, which is at the upper end of the global distribution. The TMQ distributions of grid points with higher relevance peak at even slightly higher values (although much fewer grid points are assigned high relevance). This finding is in line with our hypothesis from Sect. 5 that CG-Net learnt to associate TCs with TMQ extrema.

It is noticeable that the distributions of positive and negative relevance intervals cover similar TMQ values, however, with more relevant grid points on the positive side. This raises the question why similar values are considered in both pro and contra arguments – GG-Net could have also learnt to use *low* TMQ values as an argument against a TC feature. However, high TMQ values not only occur within TCs but also elsewhere particularly in the tropics (cf. Fig. 3a). In Sect. 5 we discussed that CG-Net is capable of learning spatial structure by means of convolution filters. We hence hypothesize that the "pro/contra TC decision" is based on spatial structure, which cannot be inferred from the relevance distributions in Fig. 7.

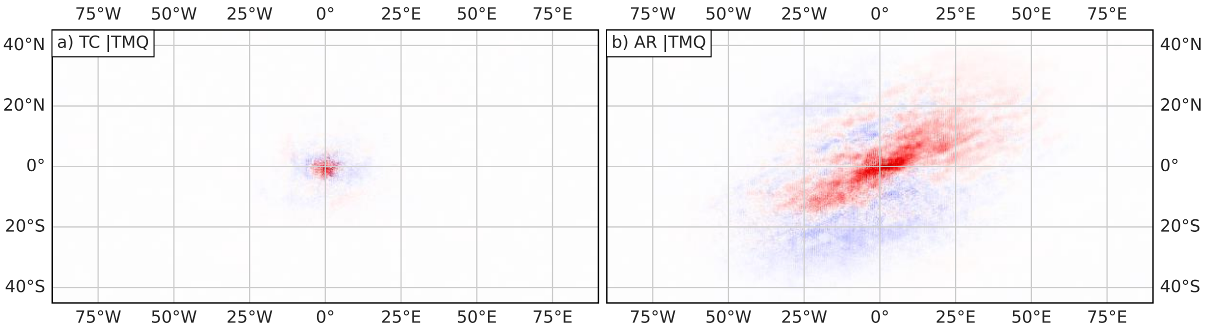

445 **Figure 8: Composite relevance maps for TMQ, averaged over (a) all TC features in the test dataset, and centred on the features. (b) The same for ARs. For clarity of presentation only AR features from the northern hemisphere are composited due to the difference in orientation on the southern hemisphere.**

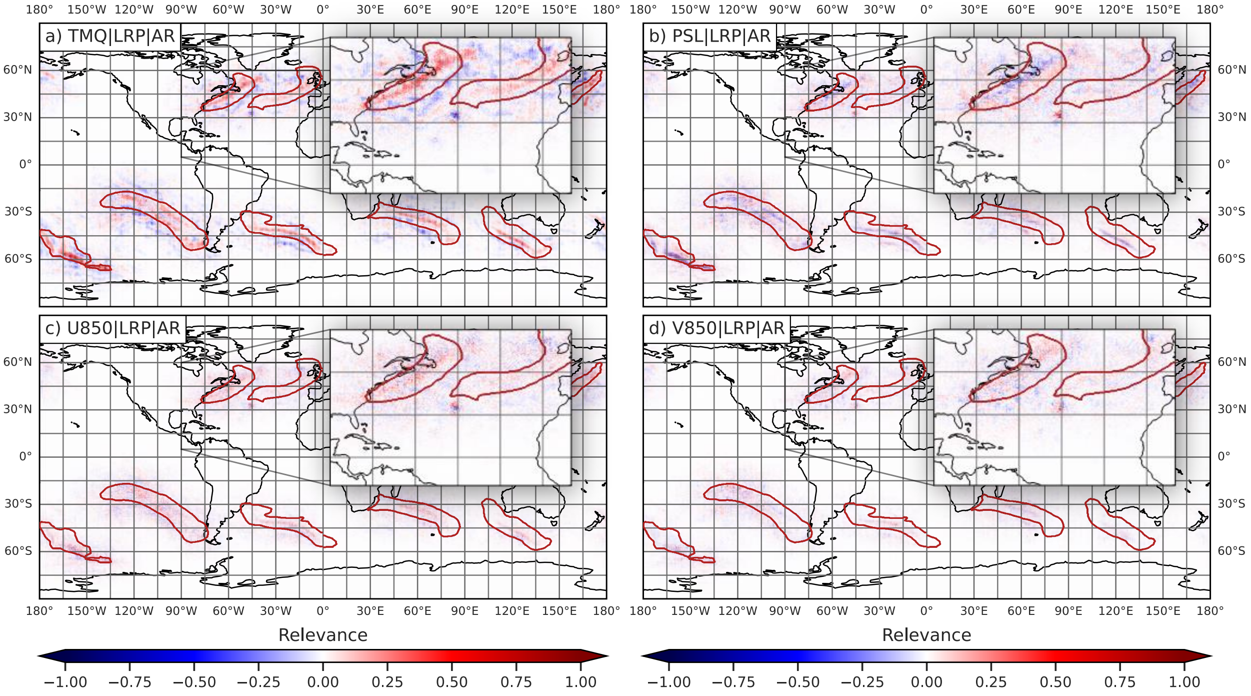

Figure 9: Same as Fig. 3g/h and Fig. 6g/h, but for relevance obtained from CG-Net trained with z-score-normalized input data
450 **shifted by +10.**

First consider the distributions shown with the blue curves in Fig. 7b. They correspond to the KS20 setup with z-score normalized data used in the previous sections. Most distributions of relevant grid points clearly differ from the global reference distributions; hence CG-Net gathers information from the values of the input variables.

To investigate, we compute composite relevance maps of all TC and AR features in the test dataset. Figure 8 shows the average relevance of TMQ for both feature classes, obtained by averaging the relevance of all features. For clarity of presentation, only AR features from the northern hemisphere are considered since their orientation differs between both hemispheres (if ARs from both hemispheres are plotted we obtain a cross-shaped pattern). Figure 8 shows that for TCs, CG-Net on average learnt to detect spherical structures. For ARs, elongated structures from south-west to north-east are detected (north-west to south-east on the southern hemisphere; not shown). We interpret this finding as strong support for the hypothesis that spatial structure plays a crucial role in the detection process. However, we note that more detailed investigation is required. Shape information is not directly accessible via LRP. To the best of our knowledge, also in general not much literature has investigated the explanation of shapes in CNN-based feature detection. While recently a potentially useful method (Concept Relevance Propagation, CRP; Achtibat et al., 2023) has been published, it has yet to be applied to meteorological data and is left for future work.

Figure 7c shows the TMQ distributions of grid points relevant for AR detection. While the distributions also show that more relevant grid points correspond to higher TMQ values (which is plausible given the discussion in Sect. 5), we here observe bi-modal distributions with minima located around the mean of the global distribution. As discussed in Sects. 4 and 5, values around the global mean become close to zero after z-score-normalization. Hence, the minimum could be a consequence of the “ignorant-to-zero-input-issue” (M22). The question hence arises whether CG-Net indeed does not consider TMQ values around the global mean of 19.3 kg m^{-2} (cf. Table 1; for which to the best of our knowledge there would be no plausible physical reason), or whether that relevance information is simply missing in LRP$_z$ output.

To investigate, we re-train CG-Net with two alternative normalizations. First, we shift the z-score-normalized data by +10. The value of 10 is chosen as minimum values after z-score normalization are about -8, hence the shift ensures that all input data are positive and at some distance from zero. Second, we apply the min-max normalization (e.g., García et al., 2014) that linearly scales all inputs to the range [0..1]. It, however, has the disadvantage of being more sensitive to outliers and cannot ensure that all inputs are treated equally important by the CNN (since the means of the different input variables are not mapped to the same normalized value; cf. Sect. 2).

IoU evaluation scores for both alternative normalizations are comparable to the original z-score normalization (e.g., AR-TC mean of 37.8 for z-score+10 and 37.7 for min-max, compared to 38.1 for the original z-score setup). Also, Fig. 7c clearly shows that with the alternative normalizations, TMQ values around the global mean *are* attributed to be relevant. The minimum in the z-score-normalization distribution vanishes and in particular for the z-score+10 data, a maximum is found instead. Hence, CG-Net *does* consider TMQ values in this range relevant.

Figure 9 revisits the case from Sect. 5 and shows AR relevance maps obtained from the CG-Net trained with z-score+10-normalized inputs. Full reproductions of Figs. 3 and 6 for both alternative normalizations are provided in the Supplement (Figs. S2-S5). Figure 9a shows that, compared to Fig. 3g, the elongated AR bands of high TMQ are still distinctly positively relevant. However, some noisy relevance is now found in the surroundings of the ARs, exactly where TMQ values around the global mean are found. We interpret this finding as further confirmation that CG-Net does consider the *values* of TMQ for feature detection, but only in combination with *shape* information.

For min-max normalization, similar results are found for the case from Sect. 5 (cf. Supplement, Figs. S4-S5). However, the relevance of TMQ values around the global mean is not as pronounced as for the shifted z-score normalization (Fig. 7c). For TC detection, the TMQ distributions hardly differ for the three normalizations (Fig. 7b). In this case, however, the relevant TMQ values are all well above the global mean (and hence already for the original z-score-normalized data above zero).

We find similarly plausible results for the other input variables. Notably, with the alternative normalizations the PSL input also shows up as relevant for TC detection (Fig. 7b). For AR detection, the PSL distributions become unimodal as for TMQ. With the alternative normalizations, however, the distributions of relevant PSL values are very similar to the global distribution. This indicates that CG-Net does not infer much information from PSL values. Since, however, the number of relevant grid points is of the same order as for the other input variables (cf. the fractions listed in Fig. 7b/c), CG-Net does use PSL inputs – likely using shape information from this field. Further evidence for this hypothesis is found in Fig. 9b, where PSL relevance also shows elongated structures aligned with the ARs.

For the U850 and V850 wind components, the bi-modal distributions of relevant wind values obtained from the original CG-Net setup (both for TCs and ARs) could have been plausible in that the CNN only considers stronger winds. However, relevance from the alternative normalizations shows that also grid points with weak winds are considered relevant. An example of this is that in Fig. 9c/d the entire AR structures show relevance, including the regions of weak wind at the southern parts of both ARs (cf. Fig. 6a/b). This relevance is not present in Fig. 6g/h; the finding again suggests that shape information used by CG-Net. The distributions in Fig. 7c show, however, that for ARs, more relevant grid points are associated with elevated eastward winds (positive U850 component). This is plausible since on both hemispheres ARs are characterized by mid-latitude eastward winds.

Concluding, the obtained distributions also provide evidence that CG-Net learnt physically plausible structures for TC and AR detection. However, due to its inability to attribute relevance from bias neurons, LRP_z applied to the original KS20 CG-Net setup using z-score normalization does not yield information about input values close to zero after normalization, which limits its use. Also, the use of shape information by the CNN cannot be attributed. Both information, however, would be required for full analysis of the learnt detection rules.

Again, reproductions of Figs. 7 and 9 when using U-Net instead of CG-Net are provided in the Supplement. For the U-Net setup, we observe that a larger number of grid points is considered relevant. However, the shape of the distributions (Fig. S8) remains similar to the CG-Net setup (Fig. 7). Also, changes in spatial relevance patterns when using the shifted z-score normalization instead of z-score normalization (Fig. S9) are analogous to the CG-Net setup (Fig. 9).

7. LRP applications: Finding most relevant input variables and evaluating detection robustness

In addition to providing a means to open the “black box” of a given CNN-based semantic segmentation setup as demonstrated in Sects. 5 and 6, we investigate further applications of LRP for semantic segmentation. Here, we discuss two applications: (A1) Finding the most relevant input variables for a given feature detection task, and (A2) evaluating the robustness of a trained detection-CNN when some characteristic of the input data is changed, e.g., grid resolution is changed, or a different geographical domain is used.

Regarding A1, P21 provided 2-D fields of 16 atmospheric variables in the ClimateNet dataset (cf. Sect. 2). Today’s numerical simulation models commonly output far more and also 3-D fields. KS20 and P21, on the other hand, used a subset of four variables only to train their CNNs (TMQ, PSL, V850, U850 and TMQ, PRECT, V850, U850), M22 only used the three inputs TMQ, V850, U850. Using a subset of available variables can be beneficial, e.g., to reduce computational complexity (data acquisition and storage; computing time and memory requirements for CNN training) and to reduce overfitting issues when only limited training data is available (e.g., Schittenkopf et al., 1997). Suitable variables can be selected based on expert knowledge (using those variables that are known to be associated with the atmospheric feature of interest, e.g., humidity and wind for TCs and ARs). However, how can suitable variables be selected if such knowledge is not readily available (e.g., for features not well investigated or if data for required variables are not available), without extensive evaluation of different variable combinations?

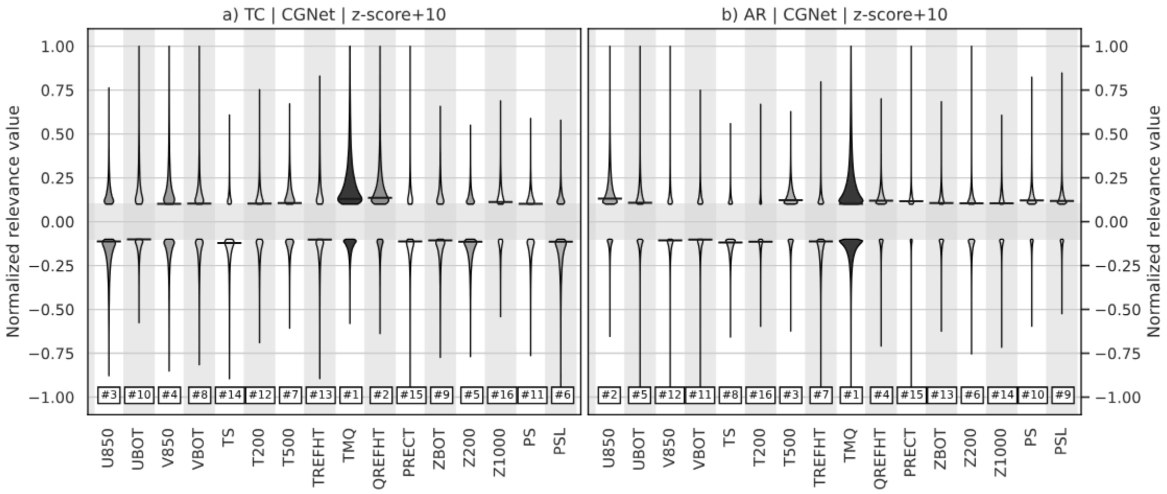

Figure 10: Distributions of relevance values (computed from test dataset) for CG-Net trained with all 16 variables contained in the ClimateNet dataset, for (a) TC and (b) AR features. Z-score normalization shifted by +10 is used on all inputs for the reasons discussed in Sect. 6. Width of violin plots is differently scaled for TCs and ARs but consistent for all variables within (a) and (b). Relevance values in the range [-0.1..0.1] are omitted. Numbers at the bottom as well as grey shade indicate ranking in terms of numbers of grid points with absolute relevance >0.1.

The analysis in Sect. 6 showed that for the different input variables, different fractions of grid points were found to be relevant in the different relevance intervals (numbers listed in Fig. 7). If a CNN is hence trained with *all* available input variables, distributions of relevance values can be computed for each input variable and the most relevant variables can be selected. We apply the approach to CG-Net trained with z-score-normalized inputs shifted by +10 (cf. Sect. 6), to avoid the "ignorance-to-zero-input-issue" (M22). Figure 10 shows violin plots (Hintze and Nelson, 1998) of the relevance distributions for each of the 16 ClimateNet variables. As in Sect. 6, we omit absolute relevance below 0.1. Variables are shown in the same order as in Table 1, the given ranking is based on the number of grid points with absolute relevance larger than 0.1.

Indeed, TMQ is found to be the most relevant input variable for both TC and AR detection. For TCs, the QREFHT variable is also considered relevant by CG-Net. However, it should be closely correlated with TMQ. U850 and V850 are third and fourth, followed by several other variables of similar relevance. Some variables including TS, PS, and Z1000 are hardly of relevance. For ARs, U850 is also considered relevant, however, V850 is not. The results suggest, however, that AR detection could benefit from including T500 in the set of input variables. These findings, of course, can be expected due to existing meteorological knowledge (Gimeno et al., 2014). It is promising, however, that LRP analysis again provides plausible results.

Table 3 shows IoU scores for CG-Net trained with all 16 input variables, the KS20 subset of TMQ, PSL, V850, U850, as well as different selections that could be inferred from Fig. 10. The scores are largely of the same order, notably the three-input subset of TMQ, V850, U850 used by M22 achieves even higher scores than the KS20 subset and the 16-variable setup. Only when even more inputs are withdrawn the detection performance drops, although remains remarkably high. We note, however, that for every setup a relevance analysis as in Sects. 5 and 6 should be carried out to ensure plausible results.

We also note that since the size of the ClimateNet dataset is limited (cf. Sects. 2 and 3), we split the data into training and test parts only (cf. Sect. 2). Relevant variables were determined based on the test data (Fig. 10). The retrained CG-Net setups in Table 3 were again evaluated on the test data. Some care needs to be taken with the results of this approach, as the variables found to be relevant could potentially be relevant mostly for the test data. If a larger dataset was available, an improved setup would split the data into three parts, also including a validation part (e.g., Bishop, 1995) for evaluating the results of the retrained setups.

Table 3: IoU scores reached by CG-Net trained for different input variable combinations, using z-score normalization shifted by +10 for all input variables. All values are in percentages. The highest score per column is written in bold. Compare to Table 2.

Input variables	AR	TC	AR-TC Mean	Background	AR-TC-BG Mean
All 16 variables listed in Table 1	**41.0**	33.7	37.4	**94.9**	56.5
TMQ-PSL-U850-V850	40.4	35.2	37.8	94.8	56.8
TMQ-QREFHT-U850-V850-T500	40.3	35.5	37.9	94.7	56.8

TMQ-T500-U850-V850	40.5	35.6	38.1	94.5	56.9
TMQ-Z200-U850-V850	40.6	**35.9**	**38.2**	94.5	**57.0**
TMQ-U850-V850	**41.0**	35.4	**38.2**	94.5	**57.0**
TMQ-U850	40.4	33.8	37.1	94.6	56.3
TMQ	39.8	30.4	35.1	94.0	54.7

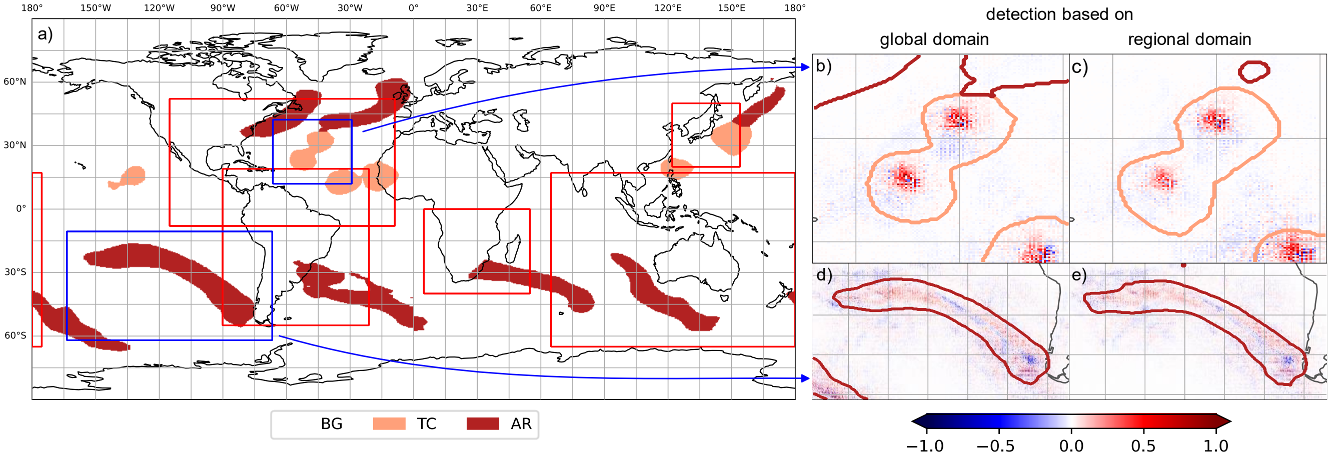

Figure 11: Regional domains to evaluate the robustness of feature detection when the CG-Net trained on global data is applied with data on a regional domain. Same case and CG-Net setup (KS20 setup and z-score normalization) as in Figs. 3 and 6. Blue bounding boxes in (a) surround selected TC and AR features; spatial relevance patterns in these regions is shown for (b, d) global data input into CG-Net, then subregion cut out from global result, and (c, e) only subregion data input into CG-Net. Note that here relevance values are summed over all variables. Red bounding boxes in (a) show domains of regional NWP models: HAFS-SAR (North Atlantic), Eta (South America), SADC region (Southern Africa), MSM (Japan), ACCESS-R (Oceania). Domains are approximate where model domains are not rectangular in longitude and latitude.

Table 4: IoU scores for TCs and ARs detection in subregions used by different regional NWP models. CG-Net with the KS20 setup and z-score normalization is used (as for Figs. 3 and 6). Scores are computed for (a) global data input into CG-Net, then subregion cut out from global result, and (b) only subregion data input into CG-Net.

Region	**(a) IoU of subregion (detection using global data)**			**(b) IoU of subregion (detection using regional data)**		
	AR	TC	BG	AR	TC	BG
Global (same as in Table 2)	40.3	35.9	94.4			
NOAA (North Atlantic)	34.5	41.1	91.7	31.2	41.0	92.3
CPTEC (South America)	41.3	43.3	92.5	34.8	38.2	92.3

SAWS (Southern Africa)	39.9	5.0	91.6	25.5	0.0	90.9
JMA (Japan)	31.5	41.0	88.9	19.1	41.6	88.3
BoM (Oceania)	38.9	10.3	91.8	36.9	4.7	92.3

Regarding A2, consider that in both operational weather forecasting and atmospheric research, numerical weather prediction (NWP) models with a regional domain are frequently used. The analysis discussed in the previous sections was based on global data. Could the CG-Net trained on global data be also used with data from a regional domain, or would it have to be retrained? The analysis of spatial relevance patterns in Sect. 5 suggested that CG-Net mostly considers grid points within or in close vicinity of a detected feature, hence we see a chance that detection with regional data could work "out of the box". This would be valuable for cases where CNN training is expensive (e.g., Niebler et al., 2022, reported high computational demand for training their front detection CNN), as a CNN trained globally could be applied to different regional models.

We consider our case from Sect. 5 and compare detected features and spatial relevance patterns (1) if the detection is based on global data as in the previous sections, then the subregion is cut out, and (2) if the detection is based on regional data input into CG-Net trained on global data. For our experiments, we simply cut out data from the global ClimateNet data, i.e., grid point spacing is unchanged. Figure 11 shows how the detection result changes for two selected TC and AR features (blue boxes in Fig. 11a). Figure 11b/d shows the features and relevance patterns when global data is used, Fig. 11c/e when regional data is used for testing. Note that for simplicity of display, the relevance of all four input variables is averaged in Fig. 11. Also note that for the regional domains, circular padding (cf. Sect. 3) is not suitable, here replicate padding is used instead.

Figure 11b-e shows that the features at the centre of the regional domains are fully detected with high similarity between both approaches. In contrast, the features only partially included in the region are not or not completely detected. These findings are plausible given that due to the convolutional architecture of CG-Net, some area around a feature is required for detection. It is noticeable, however, that the inclusion of the TC centre in the south-eastern corner of Fig. 11b/c seems to be sufficient to detect the partially included TC. This is also further evidence for our hypothesis from Sect. 5 that the distance to a TC centre plays a crucial role in the detection process. Also note that from the AR in the north-eastern part of Fig. 11b, a small part is still detected in the regional data (Fig. 11c). Unlike rule-based systems that often define a minimum size for an AR feature (Shields et al., 2018), CG-Net seems to not learn such size limitations.

The selected case provides promising evidence that indeed the CG-Net trained on global data could be used for detecting features in regional data as well. For a more complete picture, we consider several regional domains used by national weather services (red boxes in Fig. 11a): National Oceanographic and Atmospheric Administration (NOAA) in the USA (Dong et al., 2020), Center for Weather Forecasting and Climate Studies (CPTEC) in Brazil (Alves et al., 2016), South African Weather Service (SAWS; Mulovhedzi et al., 2021), Japan Meteorological Agency (JMA; Saito et al., 2006), and Australian Government Bureau of Meteorology (BoM, Puri et al., 2013). Table 4 lists IoU scores for the respective regional domains, again for feature detection based on (1) global data and (2) regional data. Despite using the same input data for detection, the IoU scores for (1) differ from the global IoU scores listed in Table 2 since only subsets of all features are present in the regional domains. Scores roughly deviate more from Table 2 for smaller subregions. For (2), IoU scores are lower compared to (1) for all subregions. This, however, is plausible considering the above discussion that features included only partially in a subregion are less well detected when only regional data is input to CG-Net. The differences in IoU scores that we observe between approaches (1) and (2) are smaller for TCs (maximum difference of 5.6% in Oceania), and more substantial for ARs (difference of up to 14.4% for the South African region and 12.4% for the Japanese region). Our hypothesis is that this is due to the smaller size of TCs, which are hence more often completely contained in a subregion. Similarly, larger regional grids show higher IoU scores, possibly for the same reason of containing more complete features.

Concluding, we note that while detection performance decreases when regional data is used for testing, we argue that the method still has value, e.g., to assist forecasters in becoming aware of potentially important features. Also, the issue of decreased detection performance for only partially contained features in a region also affects rule-based detection methods, e.g., if rules with respect to feature size are used.

Results for A1 and A2 when using U-Net instead of CG-Net are provided in the Supplement (Figs. S10 and S11; Tables S1 and S2). Both CNN architectures again yield very similar results. Notably, regarding A1, the U-Net setup also considers TMQ to be the most relevant input, however, in contrast to CG-Net the TS input provides more information.

8. Summary and conclusion

We adapted the xAI method Layer-wise Relevance Propagation, widely used in the literature for classification tasks, to be used for semantic segmentation tasks with gridded geoscientific data. We implemented the method for use with the CG-Net and U-Net CNN architectures (Fig. 1) and investigated relevance patterns these CNNs learnt for detection of 2-D tropical cyclone and atmospheric river features. Our analysis built on previous work by KS20, P21, and M22. In this paper, we focused on the CG-Net setup suggested by KS20 using the four gridded and z-score-normalized input variables TMQ, PSL, U850, V850 from the ClimateNet dataset provided by P21 (Table 1). Comparative results for U-Net are provided in the Supplement.

The main findings from our study are:

- With both CG-Net and U-Net we were able to reproduce KS20/P21 results with similar IoU scores (Sect. 3; Table 2).
- Adapting LRP (Fig. 2) to the semantic segmentation task provided the challenge of how to generalize the classification approach used by previous studies. We argue that averaging relevance from all grid points assigned to a feature provides meaningful results. Also, to use our method with the CG-Net architecture, several layer-specific LRP calculation specifications had to be implemented for CNN layers specific to CG-Net (Sect. 4).
- For the selected case, we found that CG-Net learnt physically plausible patterns for the detection task (Sect. 5). For TCs, relevant patterns include point-shaped extrema in TMQ and circular wind motion. For ARs, relevant patterns include

elongated bands of high TMQ with different orientation on northern and southern hemisphere, and eastward winds (Figs. 3 and 6).

- Spatial relevance is mostly locally confined around features, but analysis of the relevance of individual grid points indicated that for each grid point, CG-Net uses its convolutional filters to account for the surrounding region (Fig. 4).
- CG-Net makes use of both input *values* and the *shape* of patterns in the input fields. Analysis of input variable values at grid points attributed high relevance showed that, e.g., high values of TMQ are relevant for both TC and AR detection, however, that these high values are used for both *pro* and *contra* arguments for assigning a grid point to a feature (Sect. 6; Fig. 7). This behaviour can be explained by the hypothesis that CG-Net uses additional shape information for its decision. LRP does not provide information about shape relevance, however, composite maps we computed from all detected features provide strong evidence that TCs are detected as point-like structures and ARs as elongated bands (Fig. 7).
- Care needs to be taken when using LRP_z with z-score normalization (mapping the mean of a variable to zero and its standard deviation to +/- 1; as used by KS20, P21 and M22). CNNs including CG-Net and U-Net include bias neurons to account for input data close to zero, however, LRP cannot attribute relevance to bias neurons. Hence, input values close to zero are assigned a relevance close to zero (referred to as the "ignorant-to-zero-input-issue" by M22; cf. Fig. 6), even if the CNN *does* use the information via the bias neurons. As a workaround, we shifted the z-score-normalized data by +10 to avoid zero values (and also evaluated use of min-max normalization that maps variable values to 0..1). With these alternative normalizations, zero relevance around variable means disappears (Fig. 7), and spatial relevance patterns further suggest the role of shape information in the detection process (Fig. 8).
- LRP can be used for additional applications (Sect. 7). We demonstrated its use for finding the most relevant input variables to build a CNN setup by training CG-Net with all 16 input variables in the ClimateNet dataset, then using relevance distributions to find the most relevant variables that need to be retained for a useful setup (Fig. 10 and Table 3). Also, we evaluated the robustness of detection when only data from subregions is used with the CG-Net trained on global data. This has potential benefit to use a globally trained CNN for detecting features in data from regional NWP models. We find that due to the locality of relevance, features fully included in a subregion are well detected, while only partially contained features are not (Fig. 11 and Table 4).

Concluding, LRP in our opinion is a very useful tool to gain confidence for CNN-based detection of atmospheric features. For the case of TC and AR detection proposed by KS20 and P21, we find that their setup indeed learns physically plausible patterns for feature detection. We provide the source code of our implementation along with this paper and invite the geoscientific community to apply the method to further detection tasks. However, the open challenges of accounting for the relevance of bias neurons ("ignorant-to-zero-input-issue"; M22) as well as for shape information need to be approached to be able to explain the behaviour of CNNs for semantic segmentation tasks more completely. First work for accounting for bias relevance has recently been published in the computer vision literature (Wang et al., 2019), as has a method for accounting for shape information (Achtibat et al., 2023). These need to be adapted and potentially refined for geoscientific data. We look forward to future work in this direction.

Code and data availability

The code used the generate the results presented in this paper is available at https://doi.org/10.5281/zenodo.10892412. The ClimateNet dataset (P21) is also publicly available (https://doi.org/10.5281/zenodo.14046402).

Competing interests

The authors declare that they have no conflict of interest.

Author contributions

TR worked on conceptualization, data curation, formal analysis and investigation, developed the LRP code, performed the CNN training, conducted the relevance analysis, and contributed to writing of all sections. SF performed CNN training and subregion-robustness analysis, jointly worked with TR on all other analyses, and contributed to all sections, in particular to figures. CW co-supervised TR and SF, contributed to general discussion and writing, and contributed to acquiring funding (UHH Ideas and Venture Fund). IP contributed to general discussion and document editing and contributed to acquiring funding (UHH Ideas and Venture Fund). MR proposed, conceptualized and administrated study, acquired funding, supervised TR and SF; central role in discussions and writing of all sections.

Acknowledgement

The research leading to these results has been funded (a) by the Deutsche Forschungsgemeinschaft (DFG, German Research Foundation) under Germany’s Excellence Strategy – EXC 2037 'CLICCS - Climate, Climatic Change, and Society' – Project Number: 390683824, contribution to the Center for Earth System Research and Sustainability (CEN) of Universität Hamburg (UHH), (b) by DFG within the subproject “C9” of the Transregional Collaborative Research Center SFB / TRR 165 “Waves to Weather” (www.wavestoweather.de), and (c) by the UHH Ideas and Venture Fund. IP acknowledges funding from DFG, Project number 436413914.

References

Abu Alhaija, H., Mustikovela, S. K., Mescheder, L., Geiger, A., and Rother, C.: Augmented Reality Meets Computer Vision: Efficient Data Generation for Urban Driving Scenes, Int. J. Comput. Vis., 126, 961–972, https://doi.org/10.1007/s11263-018-1070-x, 2018.

Achtibat, R., Dreyer, M., Eisenbraun, I., Bosse, S., Wiegand, T., Samek, W., and Lapuschkin, S.: From attribution maps to human-understandable explanations through Concept Relevance Propagation, Nat. Mach. Intell., 5, 1006–1019, https://doi.org/10.1038/s42256-023-00711-8, 2023.

Ahmed, A. M. A. and Ali, L.: Explainable Medical Image Segmentation via Generative Adversarial Networks and Layer-wise Relevance Propagation, 2021.

Ahrens, C. D., Jackson, P. L., and Jackson, C. E. O.: Meteorology Today: An Introduction to Weather, Climate, and the Environment, Nelson Education, 710 pp., 2012.

Arras, L., Montavon, G., Müller, K.-R., and Samek, W.: Explaining Recurrent Neural Network Predictions in Sentiment Analysis, in: Proceedings of the 8th Workshop on Computational Approaches to Subjectivity, Sentiment and Social Media Analysis, WASSA 2017, Copenhagen, Denmark, 159–168, https://doi.org/10.18653/v1/W17-5221, 2017.

Avberšek, L. K. and Repovš, G.: Deep learning in neuroimaging data analysis: Applications, challenges, and solutions, Front. Neuroimaging, 1, https://doi.org/10.3389/fnimg.2022.981642, 2022.

Bach, S., Binder, A., Montavon, G., Klauschen, F., Müller, K.-R., and Samek, W.: On Pixel-Wise Explanations for Non-Linear Classifier Decisions by Layer-Wise Relevance Propagation, PLOS ONE, 10, e0130140, https://doi.org/10.1371/journal.pone.0130140, 2015.

Beckert, A. A., Eisenstein, L., Oertel, A., Hewson, T., Craig, G. C., and Rautenhaus, M.: The three-dimensional structure of fronts in mid-latitude weather systems in numerical weather prediction models, Geosci. Model Dev., 16, 4427–4450, https://doi.org/10.5194/gmd-16-4427-2023, 2023.

Beobide-Arsuaga, G., Düsterhus, A., Müller, W. A., Barnes, E. A., and Baehr, J.: Spring Regional Sea Surface Temperatures as a Precursor of European Summer Heatwaves, Geophys. Res. Lett., 50, e2022GL100727, https://doi.org/10.1029/2022GL100727, 2023.

Biard, J. C. and Kunkel, K. E.: Automated detection of weather fronts using a deep learning neural network, Adv. Stat. Climatol. Meteorol. Oceanogr., 5, 147–160, https://doi.org/10.5194/ascmo-5-147-2019, 2019.

Bishop, C. M.: Neural Networks for Pattern Recognition, Clarendon Press, 501 pp., 1995.

Bishop, C. M.: Pattern recognition and machine learning, 5. (corr. print.)., Springer, New York [u.a.], XX, 738 S. pp., 2007.

Bösiger, L., Sprenger, M., Boettcher, M., Joos, H., and Günther, T.: Integration-based extraction and visualization of jet stream cores, Geosci. Model Dev., 15, 1079–1096, https://doi.org/10.5194/gmd-15-1079-2022, 2022.

Boukabara, S.-A., Krasnopolsky, V., Penny, S. G., Stewart, J. Q., McGovern, A., Hall, D., Hoeve, J. E. T., Hickey, J., Huang, H.-L. A., Williams, J. K., Ide, K., Tissot, P., Haupt, S. E., Casey, K. S., Oza, N., Geer, A. J., Maddy, E. S., and Hoffman, R. N.: Outlook for Exploiting Artificial Intelligence in the Earth and Environmental Sciences, Bull. Am. Meteorol. Soc., 102, E1016–E1032, https://doi.org/10.1175/BAMS-D-20-0031.1, 2021.

Bourdin, S., Fromang, S., Dulac, W., Cattiaux, J., and Chauvin, F.: Intercomparison of four algorithms for detecting tropical cyclones using ERA5, Geosci. Model Dev., 15, 6759–6786, https://doi.org/10.5194/gmd-15-6759-2022, 2022.

Captum: Semantic Segmentation with Captum: https://captum.ai/tutorials/Segmentation_Interpret, last access: 17 November 2023.

Chase, R. J., Harrison, D. R., Burke, A., Lackmann, G. M., and McGovern, A.: A Machine Learning Tutorial for Operational Meteorology. Part I: Traditional Machine Learning, Weather Forecast., 37, 1509–1529, https://doi.org/10.1175/WAF-D-22-0070.1, 2022.

Chen, L.-C., Zhu, Y., Papandreou, G., Schroff, F., and Adam, H.: Encoder-Decoder with Atrous Separable Convolution for Semantic Image Segmentation, in: Computer Vision – ECCV 2018, vol. 11211, edited by: Ferrari, V., Hebert, M., Sminchisescu, C., and Weiss, Y., Springer International Publishing, Cham, 833–851, https://doi.org/10.1007/978-3-030-01234-2_49, 2018.

Cordts, M., Omran, M., Ramos, S., Rehfeld, T., Enzweiler, M., Benenson, R., Franke, U., Roth, S., and Schiele, B.: The Cityscapes Dataset for Semantic Urban Scene Understanding, in: 2016 IEEE Conference on Computer Vision and Pattern Recognition (CVPR), 2016 IEEE Conference on Computer Vision and Pattern Recognition (CVPR), Las Vegas, NV, USA, 3213–3223, https://doi.org/10.1109/CVPR.2016.350, 2016.

Dardouillet, P., Benoit, A., Amri, E., Bolon, P., Dubucq, D., and Credoz, A.: Explainability of Image Semantic Segmentation Through SHAP Values, in: Pattern Recognition, Computer Vision, and Image Processing. ICPR 2022 International Workshops and Challenges, Cham, 188–202, https://doi.org/10.1007/978-3-031-37731-0_19, 2023.

Davenport, F. V. and Diffenbaugh, N. S.: Using Machine Learning to Analyze Physical Causes of Climate Change: A Case Study of U.S. Midwest Extreme Precipitation, Geophys. Res. Lett., 48, e2021GL093787, https://doi.org/10.1029/2021GL093787, 2021.

Dawe, J. T. and Austin, P. H.: Statistical analysis of an LES shallow cumulus cloud ensemble using a cloud tracking algorithm, Atmospheric Chem. Phys., 12, 1101–1119, https://doi.org/10.5194/acp-12-1101-2012, 2012.

Dong, J., Liu, B., Zhang, Z., Wang, W., Mehra, A., Hazelton, A. T., Winterbottom, H. R., Zhu, L., Wu, K., Zhang, C., Tallapragada, V., Zhang, X., Gopalakrishnan, S., and Marks, F.: The Evaluation of Real-Time Hurricane Analysis and Forecast System (HAFS) Stand-Alone Regional (SAR) Model Performance for the 2019 Atlantic Hurricane Season, Atmosphere, 11, 617, https://doi.org/10.3390/atmos11060617, 2020.

Everingham, M., Van Gool, L., Williams, C. K. I., Winn, J., and Zisserman, A.: The Pascal Visual Object Classes (VOC) Challenge, Int. J. Comput. Vis., 88, 303–338, https://doi.org/10.1007/s11263-009-0275-4, 2010.

Farokhmanesh, F., Höhlein, K., and Westermann, R.: Deep Learning–Based Parameter Transfer in Meteorological Data, Artif. Intell. Earth Syst., 2, https://doi.org/10.1175/AIES-D-22-0024.1, 2023.

García, S., Luengo, J., and Herrera, F.: Data Preprocessing in Data Mining, Springer, 327 pp., 2014.

Gimeno, L., Nieto, R., Vázquez, M., and Lavers, D.: Atmospheric rivers: a mini-review, Front. Earth Sci., 2, 2014.

Guan, B. and Waliser, D.: Detection of Atmospheric Rivers: Evaluation and Application of an Algorithm for Global Studies, J. Geophys. Res. Atmospheres, 120, n/a-n/a, https://doi.org/10.1002/2015JD024257, 2015.

Guillemot, M., Heusele, C., Korichi, R., Schnebert, S., and Chen, L.: Breaking Batch Normalization for better explainability of Deep Neural Networks through Layer-wise Relevance Propagation, 2020.

Hengstebeck, T., Wapler, K., Heizenreder, D., and Joe, P.: Radar Network–Based Detection of Mesocyclones at the German Weather Service, J. Atmospheric Ocean. Technol., 35, 299–321, https://doi.org/10.1175/JTECH-D-16-0230.1, 2018.

Hewson, T. D. and Titley, H. A.: Objective identification, typing and tracking of the complete life-cycles of cyclonic features at high spatial resolution, Meteorol. Appl., 17, 355–381, https://doi.org/10.1002/met.204, 2010.

Higgins, T. B., Subramanian, A. C., Graubner, A., Kapp-Schwoerer, L., Watson, P. A. G., Sparrow, S., Kashinath, K., Kim, S., Delle Monache, L., and Chapman, W.: Using Deep Learning for an Analysis of Atmospheric Rivers in a High-Resolution Large Ensemble Climate Data Set, J. Adv. Model. Earth Syst., 15, e2022MS003495, https://doi.org/10.1029/2022MS003495, 2023.

Hilburn, K. A., Ebert-Uphoff, I., and Miller, S. D.: Development and Interpretation of a Neural-Network-Based Synthetic Radar Reflectivity Estimator Using GOES-R Satellite Observations, J. Appl. Meteorol. Climatol., 60, 3–21, https://doi.org/10.1175/JAMC-D-20-0084.1, 2020.

Hintze, J. L. and Nelson, R. D.: Violin Plots: A Box Plot-Density Trace Synergism, Am. Stat., 52, 181, https://doi.org/10.2307/2685478, 1998.

Holzinger, A., Saranti, A., Molnar, C., Biecek, P., and Samek, W.: Explainable AI Methods - A Brief Overview, in: xxAI - Beyond Explainable AI: International Workshop, Held in Conjunction with ICML 2020, July 18, 2020, Vienna, Austria, Revised and Extended Papers, edited by: Holzinger, A., Goebel, R., Fong, R., Moon, T., Müller, K.-R., and Samek, W., Springer International Publishing, Cham, 13–38, https://doi.org/10.1007/978-3-031-04083-2_2, 2022.

Hui, L. Y. W. and Binder, A.: BatchNorm Decomposition for Deep Neural Network Interpretation, Cham, Book Title: Advances in Computational IntelligenceDOI: 10.1007/978-3-030-20518-8_24, 280–291, https://doi.org/10.1007/978-3-030-20518-8_24, 2019.

Ioffe, S. and Szegedy, C.: Batch Normalization: Accelerating Deep Network Training by Reducing Internal Covariate Shift, in: Proceedings of the 32nd International Conference on Machine Learning, International Conference on Machine Learning, 448–456, 2015.

Justin, A. D., Willingham, C., McGovern, A., and Allen, J. T.: Toward Operational Real-Time Identification of Frontal Boundaries Using Machine Learning, Artif. Intell. Earth Syst., 2, https://doi.org/10.1175/AIES-D-22-0052.1, 2023.

Kapp-Schwoerer, L., Graubner, A., Kim, S., and Kashinath, K.: Spatio-temporal segmentation and tracking of weather patterns with light-weight Neural Networks, 2020.

Kingma, D. P. and Ba, J.: Adam: A Method for Stochastic Optimization, CoRR, 2014.

Kokhlikyan, N., Miglani, V., Martin, M., Wang, E., Alsallakh, B., Reynolds, J., Melnikov, A., Kliushkina, N., Araya, C., Yan, S., and Reblitz-Richardson, O.: Captum: A unified and generic model interpretability library for PyTorch, https://doi.org/10.48550/arXiv.2009.07896, 16 September 2020.

Labe, Z. M. and Barnes, E. A.: Predicting Slowdowns in Decadal Climate Warming Trends With Explainable Neural Networks, Geophys. Res. Lett., 49, e2022GL098173, https://doi.org/10.1029/2022GL098173, 2022.

Lagerquist, R., McGovern, A., and Ii, D. J. G.: Deep Learning for Spatially Explicit Prediction of Synoptic-Scale Fronts, Weather Forecast., 34, 1137–1160, https://doi.org/10.1175/WAF-D-18-0183.1, 2019.

Lapuschkin, S., Wäldchen, S., Binder, A., Montavon, G., Samek, W., and Müller, K.-R.: Unmasking Clever Hans predictors and assessing what machines really learn, Nat. Commun., 10, 1096, https://doi.org/10.1038/s41467-019-08987-4, 2019.

Lawrence, Z. D. and Manney, G. L.: Characterizing Stratospheric Polar Vortex Variability With Computer Vision Techniques, J. Geophys. Res. Atmospheres, 123, 1510–1535, https://doi.org/10.1002/2017JD027556, 2018.

LeCun, Y. A., Bottou, L., Orr, G. B., and Müller, K.-R.: Efficient BackProp, in: Neural Networks: Tricks of the Trade: Second Edition, edited by: Montavon, G., Orr, G. B., and Müller, K.-R., Springer, Berlin, Heidelberg, 9–48, https://doi.org/10.1007/978-3-642-35289-8_3, 2012.

Linardatos, P., Papastefanopoulos, V., and Kotsiantis, S.: Explainable AI: A Review of Machine Learning Interpretability Methods, Entropy, 23, 18, https://doi.org/10.3390/e23010018, 2021.

Liu, X., Deng, Z., and Yang, Y.: Recent progress in semantic image segmentation, Artif. Intell. Rev., 52, 1089–1106, https://doi.org/10.1007/s10462-018-9641-3, 2019.

Long, J., Shelhamer, E., and Darrell, T.: Fully convolutional networks for semantic segmentation, in: 2015 IEEE Conference on Computer Vision and Pattern Recognition (CVPR), 2015 IEEE Conference on Computer Vision and Pattern Recognition (CVPR), 3431–3440, https://doi.org/10.1109/CVPR.2015.7298965, 2015.

Lundberg, S. M. and Lee, S.-I.: A Unified Approach to Interpreting Model Predictions, in: Advances in Neural Information Processing Systems, 2017.

Mamalakis, A., Barnes, E. A., and Ebert-Uphoff, I.: Investigating the Fidelity of Explainable Artificial Intelligence Methods for Applications of Convolutional Neural Networks in Geoscience, Artif. Intell. Earth Syst., 1, https://doi.org/10.1175/AIES-D-22-0012.1, 2022.

Manakitsa, N., Maraslidis, G. S., Moysis, L., and Fragulis, G. F.: A Review of Machine Learning and Deep Learning for Object Detection, Semantic Segmentation, and Human Action Recognition in Machine and Robotic Vision, Technologies, 12, 15, https://doi.org/10.3390/technologies12020015, 2024.

MathWorks: Explore Semantic Segmentation Network Using Grad-CAM: https://de.mathworks.com/help/deeplearning/ug/explore-semantic-segmentation-network-using-gradcam.html, last access: 17 November 2023.

Mersha, M., Lam, K., Wood, J., AlShami, A. K., and Kalita, J.: Explainable artificial intelligence: A survey of needs, techniques, applications, and future direction, Neurocomputing, 599, 128111, https://doi.org/10.1016/j.neucom.2024.128111, 2024.

Mittermaier, M., North, R., Semple, A., and Bullock, R.: Feature-Based Diagnostic Evaluation of Global NWP Forecasts, Mon. Weather Rev., 144, 3871–3893, https://doi.org/10.1175/MWR-D-15-0167.1, 2016.

Montavon, G., Binder, A., Lapuschkin, S., Samek, W., and Müller, K.-R.: Layer-Wise Relevance Propagation: An Overview, in: Explainable AI: Interpreting, Explaining and Visualizing Deep Learning, edited by: Samek, W., Montavon, G., Vedaldi, A., Hansen, L. K., and Müller, K.-R., Springer International Publishing, Cham, 193–209, https://doi.org/10.1007/978-3-030-28954-6_10, 2019.

Mulovhedzi, P. T., Rambuwani, G. T., Bopape, M.-J., Maisha, R., and Monama, N.: Model inter-comparison for short-range forecasts over the southern African domain, South Afr. J. Sci., 117, https://doi.org/10.17159/sajs.2021/8581, 2021.

Narkhede, M. V., Bartakke, P. P., and Sutaone, M. S.: A review on weight initialization strategies for neural networks, Artif. Intell. Rev., 55, 291–322, https://doi.org/10.1007/s10462-021-10033-z, 2022.

Nellikkattil, A. B., O'Brien, T. A., Lemmon, D., Lee, J.-Y., and Chu, J.-E.: Scalable Feature Extraction and Tracking (SCAFET): A general framework for feature extraction from large climate datasets, EGUsphere, 1–32, https://doi.org/10.5194/egusphere-2023-592, 2023.

Neu, U., Akperov, M. G., Bellenbaum, N., Benestad, R., Blender, R., Caballero, R., Cocozza, A., Dacre, H. F., Feng, Y., Fraedrich, K., Grieger, J., Gulev, S., Hanley, J., Hewson, T., Inatsu, M., Keay, K., Kew, S. F., Kindem, I., Leckebusch, G. C., Liberato, M. L. R., Lionello, P., Mokhov, I. I., Pinto, J. G., Raible, C. C., Reale, M., Rudeva, I., Schuster, M., Simmonds, I., Sinclair, M., Sprenger, M., Tilinina, N. D., Trigo, I. F., Ulbrich, S., Ulbrich, U., Wang, X. L., and Wernli, H.: IMILAST: A Community Effort to Intercompare Extratropical Cyclone Detection and Tracking Algorithms, Bull. Am. Meteorol. Soc., 94, 529–547, https://doi.org/10.1175/BAMS-D-11-00154.1, 2013.

Niebler, S., Miltenberger, A., Schmidt, B., and Spichtinger, P.: Automated detection and classification of synoptic-scale fronts from atmospheric data grids, Weather Clim. Dyn., 3, 113–137, https://doi.org/10.5194/wcd-3-113-2022, 2022.

Pena-Ortiz, C., Gallego, D., Ribera, P., Ordonez, P., and Alvarez-Castro, M. D. C.: Observed trends in the global jet stream characteristics during the second half of the 20th century, J. Geophys. Res. Atmospheres, 118, 2702–2713, https://doi.org/10.1002/jgrd.50305, 2013.

Prabhat, Kashinath, K., Mudigonda, M., Kim, S., Kapp-Schwoerer, L., Graubner, A., Karaismailoglu, E., von Kleist, L., Kurth, T., Greiner, A., Mahesh, A., Yang, K., Lewis, C., Chen, J., Lou, A., Chandran, S., Toms, B., Chapman, W., Dagon, K., Shields, C. A., O'Brien, T., Wehner, M., and Collins, W.: ClimateNet: an expert-labeled open dataset and deep learning architecture for enabling high-precision analyses of extreme weather, Geosci. Model Dev., 14, 107–124, https://doi.org/10.5194/gmd-14-107-2021, 2021.

Puri, K., GS, D., Steinle, P., Dix, M., Rikus, L., Logan, L., Naughton, M., Tingwell, C., Xiao, Y., Barras, V., Bermous, I., Bowen, R., Deschamps, L., Franklin, C., Fraser, J., Glowacki, T., Harris, B., Lee, J., Le, T., and Engel, C.: Operational Implementation of the ACCESS Numerical Weather prediction Systems, Aust. Meteorol. Oceanogr. J., 63, 265–284, 2013.

Rahman, M. A. and Wang, Y.: Optimizing Intersection-Over-Union in Deep Neural Networks for Image Segmentation, in: Advances in Visual Computing, Cham, 234–244, https://doi.org/10.1007/978-3-319-50835-1_22, 2016.

Rautenhaus, M., Böttinger, M., Siemen, S., Hoffman, R., Kirby, R. M., Mirzargar, M., Röber, N., and Westermann, R.: Visualization in Meteorology—A Survey of Techniques and Tools for Data Analysis Tasks, IEEE Trans. Vis. Comput. Graph., 24, 3268–3296, https://doi.org/10.1109/TVCG.2017.2779501, 2018.

Ribeiro, M. T., Singh, S., and Guestrin, C.: "Why Should I Trust You?": Explaining the Predictions of Any Classifier, in: Proceedings of the 22nd ACM SIGKDD International Conference on Knowledge Discovery and Data Mining, New York, NY, USA, 1135–1144, https://doi.org/10.1145/2939672.2939778, 2016.

Ronneberger, O., Fischer, P., and Brox, T.: U-Net: Convolutional Networks for Biomedical Image Segmentation, in: Medical Image Computing and Computer-Assisted Intervention – MICCAI 2015, Cham, 234–241, https://doi.org/10.1007/978-3-319-24574-4_28, 2015.

Rueckert, D. and Schnabel, J. A.: Model-Based and Data-Driven Strategies in Medical Image Computing, Proc. IEEE, 108, 110–124, https://doi.org/10.1109/JPROC.2019.2943836, 2020.

Russell, S. and Norvig, P.: Artificial Intelligence, Global Edition, 4th ed., Pearson, Harlow, 1168 pp., 2021.

Saito, K., Fujita, T., Yamada, Y., Ishida, J., Kumagai, Y., Aranami, K., Ohmori, S., Nagasawa, R., Kumagai, S., Muroi, C., Kato, T., Eito, H., and Yamazaki, Y.: The Operational JMA Nonhydrostatic Mesoscale Model, Mon. Weather Rev., 134, 1266–1298, https://doi.org/10.1175/MWR3120.1, 2006.

Saitoh, K.: Deep Learning from the Basics: Python and Deep Learning: Theory and Implementation, Packt Publishing Ltd, 317 pp., 2021.

Schemm, S., Rudeva, I., and Simmonds, I.: Extratropical fronts in the lower troposphere–global perspectives obtained from two automated methods, Q. J. R. Meteorol. Soc., 141, 1686–1698, https://doi.org/10.1002/qj.2471, 2015.

Schittenkopf, C., Deco, G., and Brauer, W.: Two Strategies to Avoid Overfitting in Feedforward Networks, Neural Netw., 10, 505–516, https://doi.org/10.1016/S0893-6080(96)00086-X, 1997.

Selvaraju, R. R., Cogswell, M., Das, A., Vedantam, R., Parikh, D., and Batra, D.: Grad-CAM: Visual Explanations from Deep Networks via Gradient-Based Localization, in: 2017 IEEE International Conference on Computer Vision (ICCV), 2017 IEEE International Conference on Computer Vision (ICCV), 618–626, https://doi.org/10.1109/ICCV.2017.74, 2017.

Shields, C. A., Rutz, J. J., Leung, L.-Y., Ralph, F. M., Wehner, M., Kawzenuk, B., Lora, J. M., McClenny, E., Osborne, T., Payne, A. E., Ullrich, P., Gershunov, A., Goldenson, N., Guan, B., Qian, Y., Ramos, A. M., Sarangi, C., Sellars, S., Gorodetskaya, I., Kashinath, K., Kurlin, V., Mahoney, K., Muszynski, G., Pierce, R., Subramanian, A. C., Tome, R., Waliser, D., Walton, D., Wick, G., Wilson, A., Lavers, D., Prabhat, Collow, A., Krishnan, H., Magnusdottir, G., and Nguyen, P.: Atmospheric River Tracking Method Intercomparison Project (ARTMIP): project goals and experimental design, Geosci. Model Dev., 11, 2455–2474, https://doi.org/10.5194/gmd-11-2455-2018, 2018.

Simonyan, K. and Zisserman, A.: Very Deep Convolutional Networks for Large-Scale Image Recognition, in: 3rd International Conference on Learning Representations, ICLR 2015, San Diego, CA, USA, May 7-9, 2015, Conference Track Proceedings, 2015.

Sprenger, M., Fragkoulidis, G., Binder, H., Croci-Maspoli, M., Graf, P., Grams, C. M., Knippertz, P., Madonna, E., Schemm, S., Škerlak, B., and Wernli, H.: Global Climatologies of Eulerian and Lagrangian Flow Features based on ERA-Interim, Bull. Am. Meteorol. Soc., 98, 1739–1748, https://doi.org/10.1175/BAMS-D-15-00299.1, 2017.

Stull, R.: Practical Meteorology: An Algebra-based Survey of Atmospheric Science, Univ. of British Columbia, 940 pp., 2017.

Tian, Y., Zhao, Y., Son, S.-W., Luo, J.-J., Oh, S.-G., and Wang, Y.: A Deep-Learning Ensemble Method to Detect Atmospheric Rivers and Its Application to Projected Changes in Precipitation Regime, J. Geophys. Res. Atmospheres, 128, e2022JD037041, https://doi.org/10.1029/2022JD037041, 2023.

Tjoa, E., Guo, H., Lu, Y., and Guan, C.: Enhancing the Extraction of Interpretable Information for Ischemic Stroke Imaging from Deep Neural Networks, ArXiv, 2019.

Toms, B. A., Barnes, E. A., and Ebert-Uphoff, I.: Physically Interpretable Neural Networks for the Geosciences: Applications to Earth System Variability, J. Adv. Model. Earth Syst., 12, e2019MS002002, https://doi.org/10.1029/2019MS002002, 2020.

Wang, S., Zhou, T., and Bilmes, J.: Bias Also Matters: Bias Attribution for Deep Neural Network Explanation, in: Proceedings of the 36th International Conference on Machine Learning, International Conference on Machine Learning, 6659–6667, 2019.

Wehner, M. F., Reed, K. A., Li, F., Prabhat, Bacmeister, J., Chen, C.-T., Paciorek, C., Gleckler, P. J., Sperber, K. R., Collins, W. D., Gettelman, A., and Jablonowski, C.: The effect of horizontal resolution on simulation quality in the Community Atmospheric Model, CAM5.1, J. Adv. Model. Earth Syst., 6, 980–997, https://doi.org/10.1002/2013MS000276, 2014.

Wick, G. A., Neiman, P. J., and Ralph, F. M.: Description and Validation of an Automated Objective Technique for Identification and Characterization of the Integrated Water Vapor Signature of Atmospheric Rivers, IEEE Trans. Geosci. Remote Sens., 51, 2166–2176, https://doi.org/10.1109/TGRS.2012.2211024, 2013.

Wu, T., Tang, S., Zhang, R., Cao, J., and Zhang, Y.: CGNet: A Light-Weight Context Guided Network for Semantic Segmentation, IEEE Trans. Image Process., 30, 1169–1179, https://doi.org/10.1109/TIP.2020.3042065, 2021.

Xie, E., Wang, W., Yu, Z., Anandkumar, A., Alvarez, J. M., and Luo, P.: SegFormer: Simple and Efficient Design for Semantic Segmentation with Transformers, in: Advances in Neural Information Processing Systems, 12077–12090, 2021.

Zhou, B., Zhao, H., Puig, X., Fidler, S., Barriuso, A., and Torralba, A.: Scene Parsing through ADE20K Dataset, in: 2017 IEEE Conference on Computer Vision and Pattern Recognition (CVPR), 2017 IEEE Conference on Computer Vision and Pattern Recognition (CVPR), Honolulu, HI, 5122–5130, https://doi.org/10.1109/CVPR.2017.544, 2017.